Submitted to *J. Geophys. Res.*: June 1, 2004.

Stratification of Anisotropy in the Pacific Upper Mantle

Daniel B. Smith, Michael H. Ritzwoller†, Nikolai M. Shapiro

Center for Imaging the Earth's Interior

Department of Physics

University of Colorado

Campus Box 390, Boulder, CO 80309-0390, USA

† To whom correspondence should be directed: ritzwoller@ciei.colorado.edu

Abstract

Based on the use of broad-band (25 sec - 150 sec) Rayleigh wave group speeds to estimate the 2ψ component of azimuthal anisotropy, we present evidence for a stratification of anisotropy in the uppermost mantle at large-scales across the Pacific basin. We confirm previous surface wave studies that established that the fast-axis directions of azimuthal anisotropy for intermediate and long period Rayleigh waves approximately align with present-day plate motions. At shorter periods (25 sec - 50 sec), however, fast-axes align nearer to the paleo- or fossil spreading direction which differs from present-day plate motion in the old Pacific. These observations, together with the age dependence of the amplitude of azimuthal anisotropy, imply that azimuthal anisotropy in the Pacific upper lithosphere ($<$ 100 km depth) is fixed or "fossilized", on average, reflecting the strain conditions extant during the early evolution of the lithosphere rather than the current ambient flow direction. In the deeper lithosphere and asthenosphere, anisotropic fast axis directions align nearer to present-day plate motions, apparently having re-oriented to conform to the current conditions of flow. The anisotropy of the shallow lithosphere may be fixed because the shear strains that can produce a change in anisotropy occur at increasing depths as the plate ages.

1. Introduction

A large body of evidence has established that seismic wave propagation in the Earth's uppermost mantle is anisotropic. At large scales, much of this evidence has derived from surface wave dispersion, although anisotropy in S_n and P_n travel times has played a centrally important role in establishing the anisotropic character of the oceanic upper mantle (e.g., Hess, 1964; Raitt et al., 1969; Shearer and Orcutt, 1986) and strenuous efforts have been devoted to the study of shear wave splitting to image smaller-scale variations in anisotropic structure (e.g., Savage, 1999 for a review).

There are two general types of surface wave anisotropy that have been observed. The first is that vertically polarized surface waves propagate more slowly than horizontally polarized waves in the uppermost mantle (e.g., Aki and Kaminuma, 1963; McEvilly, 1964, and many others) and regionally in the crust (e.g., Shapiro et al., 2004). This "Rayleigh-Love discrepancy" indirectly implies widespread radial anisotropy (transverse isotropy with a vertical symmetry axis) whose strength varies over the Earth's surface (e.g., Ekström and Dziewonski, 1998). Radial anisotropy has been a common feature of both 1-D (e.g., Dziewonski and Anderson, 1981) and 3-D (e.g., Nataf et al., 1984) mantle models for the past two decades. The second type of surface wave anisotropy is the variation of surface phase speeds with azimuth (e.g., Forsyth, 1975; Nishimura and Forsyth, 1989; Montagner and Tanimoto, 1991; Ekström, 2000; Trampert and Woodhouse, 2003) which provides direct evidence for azimuthal anisotropy where the fast axis of propagation lies in the horizontal plane. Inverting for azimuthal anisotropy is difficult, however, as the variables that describe it must be introduced to an isotropic inverse problem which is already underdetermined. The amplitude of the azimuthal terms depends strongly on the damping and regularization applied to the inversion (e.g., Barmin et al., 2001), which makes the strength of azimuthal anisotropy, in particular, difficult to estimate. Inferences, therefore, must necessarily concentrate on patterns of azimuthal anisotropy and perhaps relative lateral amplitude variations.

Radial and azimuthal anisotropy of surface waves have a common cause, the underlying anisotropy of rocks in the Earth's mantle. Anisotropy in upper mantle rocks can be explained by the accumulation of strain due to mantle convection (e.g., McKenzie, 1979) which manifests itself as lattice preferred orientation (LPO) of mantle minerals, in particular olivine (e.g.,

Babuska and Cara, 1991, for a review). This clustering of crystallographic axes around a particular orientation is typically referred to as mineralogical *fabric*. Only a modest alignment of olivine is needed to produce commonly observed mantle anisotropy strengths of 2 - 6% (Ribe and Yu, 1992). The interest in seismic anisotropy, therefore, is that, at least in principal, observations of anisotropy can be used to constrain mantle flow (e.g., McKenzie, 1979; Regan and Anderson, 1984; Tanimoto and Anderson, 1984; Ribe, 1989; Chastel et al., 1993; Russo and Silver, 1994; Tommasi, 1998; Buttles and Olson, 1998; Hall et al., 2000; Blackman and Kendall, 2002; Blackman et al., 2002; Becker et al., 2003; Gaboret et al., 2003). To date, the most straightforward results have been obtained in relatively young oceanic areas where the direction of the fast axis of azimuthal anisotropy is approximately aligned with the spreading direction (e.g., Hess, 1964; Raitt et al., 1969; Morris et al., 1969; Shearer and Orcutt, 1986; Wolfe and Solomon, 1998). This alignment has been taken as evidence for the near-horizontal shearing of the uppermost oceanic mantle in the direction of plate motion, approximately perpendicular to the mid-oceanic ridge. This idea is supported by theoretical studies (e.g., Ribe, 1992; Kaminski and Ribe, 2001; Blackman et al., 2002) and laboratory measurements (e.g., Zhang and Karato, 1995) suggesting that the fast axis of olivine tends to align nearly parallel to the direction of shear.

These results have led to a simple model that postulates that the observed fast axis of seismic anisotropy beneath oceans is, on average, close to the the direction of shear or to the largest axis of the finite-strain ellipsoid associated with on-going mantle flow. Under this interpretation, azimuthal anisotropy can be used as proxy for the pattern of mantle flow and observations of shear-wave splitting (e.g. Russo and Silver, 1994; Peyton et al., 2001; Silver and Holt, 2002) and surface-wave azimuthal anisotropy (e.g., Gaboret et al., 2003; Becker et al., 2003) have been used to infer regional and global flow patterns.

There are several reasons to be cautious with this postulated interpretation of seismic anisotropy as a proxy for mantle flow. First, in most areas the observed seismic anisotropy is more complicated than a system with a fast horizontal axis of symmetry, and requires additional radial anisotropy which has a vertical slow axis of symmetry (e.g., Ekström and Dziewonski, 1998; Shapiro and Ritzwoller, 2002). Evidence for a depth-dependent distribution of anisotropy has been found both beneath continents (e.g., Savage and Silver, 1994; Levin

et al., 1999; Vinnik et al., 2002) and oceans (e.g., Wolfe and Solomon, 1998). Second, the formation and evolution of mantle anisotropy in response to deformation is a complex process that depends on the thermal history and composition of the upper mantle. It has been argued, for example, that some observations of seismic anisotropy are attributable to fossil mineralogical fabric (e.g., Wolfe and Solomon, 1988) or to the presence of water in the upper mantle that can result in a fast anisotropy axis nearly perpendicular to the flow direction (e.g., Jung and Karato, 2001).

This paper aims to test the hypothesis that at large scales azimuthal anisotropy can be used as an indicator for mantle flow beneath oceans and its corollary that water in the upper mantle is not strongly affecting the relation between mantle flow and seismic anisotropy. We estimate the distribution of azimuthal anisotropy across the Pacific by inverting surface-wave dispersion data. We focus on the Pacific for three reasons. First, because the oceanic crust is thin the anisotropy of oceanic crustal minerals does not obscure estimates of mantle anisotropy as strongly as does the anisotropy of the much thicker continental crust. Second, both the present-day plate kinematics and the past tectonic history of the Pacific are relatively well understood. Third, the natural distribution of seismicity around the Pacific provides relatively good path and azimuthal coverage and, as we will show below, robust large-scale patterns of azimuthal anisotropy can be inferred from the inversion of surface waves crossing the Pacific. Figure 1a presents the contour that defines what we refer to as "the Pacific". It includes parts of the Nazca, Cocos, Juan de Fuca and Antarctic Plates in addition to most of the Pacific Plate where lithospheric age is well determined (Mueller et al., 1997).

There have already been numerous studies of surface-wave azimuthal anisotropy across the Pacific (e.g., Montagner and Tanimoto, 1991; Montagner, 1998; Ekström, 2000; Trampert and Woodhouse, 2003; Becker et al., 2003). These studies generally agree that in the young Pacific anisotropic fast axes tend to align with present-day plate motions, lying nearly perpendicular to the East Pacific Rise, but all have been based on relatively long period (greater than ~ 40 sec) surface wave phase speeds which provide rather poor vertical resolution. In contrast, we apply a large, newly compiled set of group speed observations that are measured down to periods of $\sim$20 sec, which improves depth resolution in the uppermost mantle.

As described below, we confirm previous surface wave studies that established that the

fast-axis directions of azimuthal anisotropy for intermediate and long period ($>\sim$ 50 sec) Rayleigh waves approximately align with present-day plate motions. We show, however, that at shorter periods fast-axes align nearer to the paleo-spreading direction. This suggests that anisotropy in the shallow upper mantle is "frozen in" or "fossilized" and represents the conditions of formation of the lithosphere rather than the current ambient flow direction. Below the shallow lithosphere, fast axis directions more nearly conform to present-day plate motions. A similar two-layered system of anisotropy has been suggested to explain observations of shear-wave splitting near Hawaii (Wolfe and Solomon, 1988).

In section 2, we describe the group velocity data set and the method of inversion used to produce maps of azimuthal anisotropy across the Pacific. The results of the inversion are presented in section 3 and their meaning is discussed in section 4.

2. Data and Method of Inversion

2.1 Data

The data set consists of Rayleigh wave group and phase speed measurements obtained from global and regional networks. Ritzwoller and Levshin (1998) describe the data selection and group velocity measurement procedures. Globally, measurements have been obtained for more than 200,000 individual minor arc paths. There are no group velocity measurements for major arc paths. After a preliminary elimination of outliers based on summary-ray analysis, the data are "cleaned" by rejecting measurements whose observed travel times greatly disagree with travel times predicted by the 3-D model of Shapiro and Ritzwoller (2002). About 98% of the original observations are retained, resulting in 28,800, 28,100, 19,700, and 11,600 group velocity measurements at periods of 25, 50, 100, and 150 sec, respectively, that cross some part of the Pacific basin. The resulting path density is shown in Figure 1. Path density degrades appreciably above about 100 sec period and is regionally worst in the central, eastern Pacific. Path density over large expanses of the very young and the very old Pacific, which we will contrast and on which we will concentrate interpretation, is adequate, however, except arguably at very long periods.

We also have a data set of about 40,000 Rayleigh wave phase speed observations measured at Utrecht University (Trampert, personal communication, 2003) at periods ranging from 40

- 150 sec. The phase speed maps include both major and minor arc measurements that are inverted jointly (Levshin et al., 2004) for comparison with the group speed results. This data set consists of about 11,500 minor-arc and 6,000 major-arc measurements that cross some part of the Pacific basin. In contrast with the number of group velocity measurements for which the frequency band of measurement was chosen interactively by an analyst, the number of phase velocity measurements is approximately constant with period. Phase velocity measurements result from an automated procedure that produces a measurement only if the acceptance criteria are passed at all periods in the frequency band of interest (∼40 - 150 sec).

2.2 Surface Wave Tomography

The azimuthal dependence of local phase (Smith and Dahlen, 1973; Romanowicz and Snieder, 1988; Larsen et al., 1998) and group speed in the presence of a weak general anisotropy is given by

$$c(r,\psi) = c_I(r) + c_A(r,\psi) \quad (1)$$

$$c_I(r) = A_0(r) \quad (2)$$

$$c_A(r,\psi) = A_1(r)\cos(2\psi) + A_2(r)\sin(2\psi) + A_3(r)\cos(4\psi) + A_4(r)\sin(4\psi), \quad (3)$$

where c_I and c_A are the local isotropic and azimuthally anisotropic parts of the wave speed, respectively, A_0 is the isotropic coefficient, $A_1, \ldots, A_4$ are the anisotropic coefficients, and ψ is the local azimuth. The coefficients $A_0, \ldots, A_4$ depend on period and wave type (Rayleigh/Love). The tomography procedure to estimate $A_0, \ldots, A_4$ is described by Barmin et al., (2001). The method minimizes a penalty functional that can be represented schematically as follows:

(two-norm weighted misfit)

$+ \alpha_i$ (isotropic spatial smoothness(σ_i)) $+ \alpha_a$ (anisotropic spatial smoothness(σ_a))

$+ \beta$ (deviation from input model(ρ)).

The weights in the misfit component of the penalty functional are the inverse of the measurement uncertainties. There are three trade-off parameters, α_i, α_a and β that weight the smoothness of the isotropic and anisotropic parts of the model and impose an explicit

constraint on model norm in regions of poor data coverage. The smoothness constraint also depends on a spatial smoothing length or spatial correlation length parameter, σ, which is the standard deviation of the Gaussian spatial smoothing operator. A different correlation length is used for the isotropic (σ_i) and anisotropic (σ_a) parts of the model. The model norm constraint depends adaptively on the local path density, ρ. If the local path density is greater than about 50 paths for a given $2^\circ \times 2^\circ$ cell, the model-norm constraint vanishes. Except for small regions at 150 sec period, path density is everywhere greater than this cut-off value so the model norm constraint is not applied. In practice, therefore, there are four "damping parameters" applied in the inversion: α_i and σ_i that control the nature of the isotropic model and α_a and σ_a that control the anisotropic part of the model. We typically refer to the α parameters as the "damping" parameters and the σ parameters as the "smoothing" parameters, although in fact each parameter acts both to damp amplitudes and smooth the resulting maps. The effect of varying these parameters will be discussed in section 2.3 following.

The estimated model is defined relative to a radially anisotropic reference model, which at each period and wave-type is the dispersion map computed from the 3-D model of Shapiro and Ritzwoller (2002) that has been updated and described by Ritzwoller et al. (2004) for the Pacific. In each inversion, the isotropic, the 2ψ, and the 4ψ coefficients are estimated simultaneously, but we will concentrate our discussion exclusively on the 2ψ maps for Rayleigh waves. We define the amplitude of the 2ψ component of azimuthal anisotropy at position $\mathbf{r}$ to be:

$$A_{2\psi}(\mathbf{r}) = \frac{c_A^{max}(\mathbf{r}) - c_{ref}(\mathbf{r})}{c_{ref}(\mathbf{r})} = \frac{\sqrt{A_1^2(\mathbf{r}) + A_2^2(\mathbf{r})}}{c_{ref}(\mathbf{r})}, \tag{4}$$

where A_1 and A_2 are the 2ψ anisotropy coefficients from equation (3), c_{ref} is the reference model speed, and c_A^{max} is the maximum speed with respect to ψ.

The inversion procedure of Barmin et al. (20021has been modified to include spatially extended surface wave sensitivity kernels for both minor arc (Ritzwoller et al., 2002) and major arc surface waves (Levshin et al., 2004). We refer to the use of these finite frequency kernels as "diffraction tomography", in contrast with "ray theory" which assumes that surface wave sensitivity is confined to an infinitesimally wide great-circle linking source and receiver. The inversions shown here are based on diffraction tomography for the isotropic part (A_0), but ray theory for the anisotropic coefficients ($A_1, \ldots, A_4$). We use ray theory for the anisotropic

part of the model because the diffraction theory for anisotropy remains unclear to us. In particular, when using diffraction tomography to compute travel times through an azimuthally anisotropic model the local azimuth at the scatterer is not uniquely defined. By considering various alternative choices for the local azimuth, we argue in the Appendix that, at least for the Pacific, diffraction effects will not modify the characteristics of the anisotropic model that we interpret here. Ray theory for anisotropic part of the model, therefore, will be sufficiently accurate for our purposes.

The inversion is global. The isotropic part of the model is represented on a $2^\circ \times 2^\circ$ spatial grid, but the anisotropic part of the model is on a $5^\circ \times 5^\circ$ grid.

2.3 Choice of Damping and Smoothing

The damping parameters α_i and α_a and the smoothing parameters σ_i and σ_a together determine the amplitude and smoothness of the perturbation from the input reference model. We show here that over a broad range of parameters the large-scale spatial pattern of azimuthal anisotropy across the Pacific is robust, but the amplitude of anisotropy is largely undetermined. The relative amplitude of azimuthal anisotropy, for example as a function of lithospheric age, is fairly robust, but is not as well determined as the pattern. All comments we make here about damping and smoothing hold for estimating azimuthal anisotropy only across the Pacific.

We find, but due to space limitations do not show here, that at large spatial scales such that $\sigma_a > 10^3$ km, the spatial pattern and relative amplitude of azimuthal anisotropy are robust relative to: data subsetting into two randomly selected equally sized data subsets, the use of ray theory versus diffraction theory for the isotropic part of the model, and changes across a broad range of isotropic damping (α_i) and smoothing (σ_i) parameters. In particular, the pattern and relative amplitude of azimuthal anisotropy are robust even when we allow the isotropic part of the model to have unphysically large amplitudes and much short wavelength structure. Because the choice of the isotropic smoothing and damping parameters are of little consequence to the anisotropy results presented below, we fix $\sigma_i = 300$ km and the relative value of $\alpha_i = 4/3$. (The values of α_i and α_a reported here are only relative values, defined such that $\alpha_a \sim 1$ in the middle of the band of "acceptable" damping parameters discussed below.)

As shown in the Appendix, the spatial pattern and relative amplitude of azimuthal anisotropy are also robust at large-scales to the choice of the use of ray theory versus diffraction theory for the anisotropic part of the model.

The situation is more troublesome with respect to the choice of the anisotropy damping (α_a) and smoothing (σ_a) parameters. If σ_a, the anisotropy correlation length, is much smaller than $\sim 10^3$ km, the spatial pattern of anisotropy tends to become chaotic and is susceptible to relatively small changes in the other parameters in the inversion. Thus, only the large scale pattern of anisotropy can be resolved with confidence and we fix $\sigma_a = 10^3$ km in all subsequent results.

The choice of the damping parameters in some inversions can be guided by fit to the data. Unfortunately, misfit is not a reliable guide to the choice of the anisotropy damping parameter as only small improvements in fit to the data are afforded by changing α_a. For example, as Figure 2 illustrates, reducing α_a by an order of magnitude from 10/3 to 1/3 will change rms-misfit for the 50 sec Rayleigh wave group speed only from 16.0 sec to 15.3 sec. This lower value can be attained as well by reducing isotropic damping.

Tighter constraints on the choice of the anisotropy damping parameter derive by considering the amplitude of anisotropy. Figure 3 shows that α_a can vary over a broad-range and for the 50 sec Rayleigh wave group speed will produce an average amplitude of anisotropy of less than about 1% with peak amplitudes less than about 4%. This range includes values of α_a as small as about 1/3. If α_a is larger than about 3, then the amplitude of azimuthal anisotropy becomes increasingly negligible. We, therefore, will restrict α_a to lie within the order of magnitude from 1/3 to 10/3. Similar assessments at different periods result in the same range of allowed values for α_a. We seek inferences that are common to all maps with the anisotropic damping parameter α_a in this band.

3. Results

As discussed in section 2, we seek inferences that are common to all maps of azimuthal anisotropy in which the anisotropic smoothing parameter $\sigma_a = 10^3$ km and the anisotropic damping parameter $\alpha_a \in [1/3, 10/3]$. These parameters have been chosen to provide robustness relative to arbitrary choices of the damping parameters and to ensure that the peak amplitude

of the resulting anisotropy maps are physically reasonable.

Figure 4 displays selected maps of azimuthal anisotropy from this range of anisotropic smoothing and damping parameters for the 50 sec Rayleigh wave group speed. There are prominent differences among these maps; in particular, as noted before (Fig. 3) the amplitude of anisotropy changes appreciably as a function of α_a. There are, however, common features that we argue here are worthy of interpretation. In particular, the large-scale pattern of anisotropy across the Pacific is similar in each case. This can be illustrated by use of the "coherence function" K(δ) introduced by Griot et al. (1998). This function is a measure of the spatial similarity between the patterns of azimuthal anisotropy in two maps and is defined as follows:

$$K(\delta) = \frac{\sum_{\theta}\sum_{\phi} U_1(\theta,\phi)U_2(\theta,\phi)\sin(\theta)\exp\left(-\frac{(\psi_{max,1}(\theta,\phi)-\psi_{max,2}(\theta,\phi)+\delta)^2}{2D_{corr}^2}\right)}{\left(\sum_{\theta}\sum_{\phi}\sin(\theta)U_1^2(\theta,\phi)\right)^{1/2}\left(\sum_{\theta}\sum_{\phi}\sin(\theta)U_2^2(\theta,\phi)\right)^{1/2}}. \quad (5)$$

$U_1(\theta,\phi)$ and $U_2(\theta,\phi)$ are the amplitudes of the two maps at each point (θ,ϕ) where θ is the co-latitude and ϕ is the longitude, and where $U = \sqrt{A_1^2 + A_2^2}$ such that the anisotropy coefficients A_1 and A_2 are defined by equation (3). D_{corr} is the uncertainty in the direction of anisotropy, which we set to 10°, and determines the width of the coherence function. Equation (5) measures the correlation between two maps when one is rotated by angle δ relative to the other. We compute coherence only across the Pacific, effectively setting anisotropy outside the Pacific to zero.

If two maps correlate perfectly, K(δ) will appear as a narrow symmetric Gaussian-shaped function centered on $\delta = 0$ with unit amplitude. An example is presented in Figure 5a, which is the coherence between two 50 sec Rayleigh wave group speed maps estimated with α_a of 1/3 and 1, respectively. These are the two maps shown in Figures 4a and 4b. The coherence function is relatively narrow, peaks near to the origin, and is approximately symmetric about the origin. When the coherence function does not display multiple maxima, we can summarize the result by the value of the peak coherence, which in the example in Figure 5a is about 0.75. Peak coherence is displayed for a wide range of anisotropy damping parameters α_a in Figure 5b. For $\alpha_a \in [1/3, 10/3]$, coherence is high, consistent with what can be ascertained by visual comparison within Figure 4, that the large-scale spatial pattern of anisotropy across

the Pacific is robust. This result is only for the 50 sec Rayleigh wave group speed, but similar results are obtained at the other periods for both group and phase speeds.

Although the absolute amplitude of azimuthal anisotropy is not robust relative to physically reasonable variations in the damping of anisotropy, α_a, the relative amplitude of anisotropy across the Pacific is more stable, as Figure 6 illustrates. For the 50 sec Rayleigh wave group speed, the strength of anisotropy nearly halves on average from the ridge to a lithospheric age of about 125 Ma and then flattens or slightly increases. Reducing α_a increases the variance within each age bin, but the trend remains in the bin means. At the weakest damping ($\alpha_a \sim 1/3$), strong small-scale anisotropy is introduced in the far western Pacific east of the Philippine Plate that is below the resolution at larger values of the damping parameter.

Figure 7 shows maps of the 2ψ component of azimuthal anisotropy for Rayleigh wave group speeds at four periods: 25 sec, 50 sec, 100 sec, and 150 sec. These maps derive from the value of α_a in the middle of the range of accepted values; i.e., $\alpha_a = 1$. Amplitudes generally decrease with period, but it is difficult to compare amplitudes quantitatively across periods because absolute amplitudes are poorly constrained. The patterns of anisotropy at long-periods (100 sec, 150 sec) are very similar, but the shorter period maps (25 sec, 50 sec) disagree with the longer period maps, particularly in the western Pacific. This can be seen more clearly in the peak coherence values listed in Table 1. We will show below that long period fast-axis directions align with present-day plate motions across the entire Pacific. At shorter periods, however, they align well with present day plate motions only in the young Pacific.

The 2ψ component of the 50 sec Rayleigh phase speed map (not shown here) that we estimated for the Pacific displays strong visual agreement with the maps presented by Trampert and Woodhouse (2003) from a nearly identical data set. Our tomography procedure, therefore, yields similar results to theirs even though the methodology is very different. Direct comparison between group and phase speed maps is difficult because the waves sample the earth differently. Figure 8 displays Rayleigh wave group and phase speed sensitivity kernels to isotropic shear wave speed, which are very similar to the sensitivity kernels for anisotropic shear wave speed (Becker et al., 2003). The Rayleigh wave group speed sensitivity kernels peak at about 30 km, 50 km, 90 km, and 140 km for 25 sec, 50 sec, 100 sec, and 150 sec period,

respectively. The phase sensitivity kernels peak deeper at each period (70 km, 125 km, and 200 km at 50 sec, 100 sec, and 150 sec) and are heavier-tailed with depth. The negative lobe on the group speed kernels, in particular, makes direct comparison between group and phase speed maps is difficult, although the best comparison between the group and phase speed maps is probably between the 50 sec phase and 100 sec group maps. Comparison reveals that the 2ψ component of azimuthal anisotropy on these maps is probably as similar as can be expected given the differences in wave sensitivities and size of the data sets.

4. Discussion

4.1 Comparison Between 2ψ Fast Axis Directions and Present-Day Plate Motions

Previous studies of the azimuthal anisotropy of Rayleigh wave phase speeds between about 40 sec and 150 sec period across the Pacific have noted that 2ψ fast axis directions align approximately with present-day plate motions. This is particularly striking near the East Pacific Rise where fast axis directions are oriented nearly perpendicular to the ridge. We test this hypothesis with the Rayleigh wave group speed maps from 25 sec to 150 sec period (Fig. 7) by comparing with the present-day plate motion model HS3-NUVEL-1A of Gripp and Gordon (2002) shown in Figure 9. As Figure 8 illustrates, the short period group velocities provide much more sensitivity to anisotropy in the shallow uppermost mantle than the intermediate and long period phase speeds. The results of this comparison are shown in Figures 10 - 12.

We map the difference in azimuth between the direction of present-day plate motion and the anisotropic fast axis direction for Rayleigh wave group speed from 25 sec to 150 sec period in Figure 10. At long periods, particularly at 150 sec, the 2ψ fast axis directions align with the present day plate directions across most of the Pacific. Notable exceptions occur mainly near discontinuities in the plate motion model where the seismic model cannot resolve rapid spatial changes; e.g., near the Tonga-Fiji arc and along the Pacific-Antarctic Ridge. As periods reduce below 150 sec, however, there is a systematic deviation from present-day plate motions. Figure 11 demonstrates this with normalized weighted histograms of the azimuth differences. The weighted azimuth differences are also plotted versus lithospheric age in Figure 12. At 150 sec, although there is a slight trend with increasing lithospheric age, the anisotropic fast axes lie within about 20° of current plate directions irrespective of the age of the lithosphere. At

shorter periods, the discrepancy with lithospheric age increases. Note, however, that even at 25 sec period the anisotropic fast axis directions, on average, lie within 20°-25° of current plate motion directions in the young Pacific. At 25 sec period it is clear that the deviation grows most rapidly after an age between 40 and 70 Ma. A similar on-set time for the deviation of the direction of anisotropy from present plate motion appears to be present but is more subtle at longer periods.

In conclusion, although at all periods group velocity anisotropic fast axis directions are aligned with present day plate motions in the young Pacific, only the very long period group speeds maps have fast axis directions oriented with current plate motions in the old Pacific. At shorter periods, which are more sensitive to the shallow lithosphere, fast axis directions in the old Pacific are significantly different from the present plate directions.

4.2 Comparison Between 2ψ Fast Axis Directions and Paleo-Spreading Directions

If the anisotropic directions at short periods are not oriented along the direction of current plate motions in the old Pacific, what does or has controlled their orientation? It turns out that the anisotropic fast axis directions for the shorter period maps align more closely with the direction the plate was moving at the time of its formation.

To estimate this direction we compute the "paleo-spreading direction" from the gradient of lithospheric age. The direction of the local gradient of the lithospheric age A will coincide with the paleo-spreading direction everywhere but near age boundaries, such as transform faults or the mid-oceanic ridge where the direction of the local age gradient is unstable even though its magnitude can be very large. Therefore, to estimate an average paleo-spreading direction in a particular region, the points located in the vicinity of plate boundaries must be excluded from the analysis. As a practical matter, we estimated the regional average paleo-spreading directions using the following two-step procedure. First, we computed the local age gradient $\nabla A(\mathbf{r})$ at each point $\mathbf{r}$ on a 0.1° grid from the compilation of lithospheric age by Mueller et al. (1997). In the second step, we used the gradient to compute the weighted two-dimensional covariance matrix in a moving two-dimensional Gaussian window $G(\mathbf{r})$:

$$C_{xy}(\mathbf{r}) = \int_S \nabla_x A(\mathbf{r}')\nabla_y A(\mathbf{r}')G(|\mathbf{r}-\mathbf{r}'|)w(\mathbf{r}')d\mathbf{r}'^2 \qquad (6)$$

where $\sigma = 1500$ km in the Gaussian window (close to the lateral resolution for azimuthal

anisotropy), the subscripts x, y denote the x and y components of the gradient vector and the covariance matrix, and the weight $w(\mathbf{r}')$ approaches zero when the amplitude of the age gradient is either very large (e.g., near transform faults) or very small (i.e., if the age gradient is poorly defined). The regional average paleo-spreading direction is defined as the direction of the eigenvector of the matrix $\mathbf{C}$ corresponding to its larger eigenvalue. We refer to this as a spreading direction rather than plate motion because it only represents the component of plate motion perpendicular to the ridge. The component of plate motion parallel to the ridge is not revealed by taking the gradient of the age.

The final estimate of the local paleo-spreading directions is shown in Figure 13. Comparison with present day plate motion in Figure 9 shows that the paleo-spreading directions are similar to plate motion in the young Pacific, but deviate significantly in the old Pacific. More detailed inspection reveals that the paleo-spreading directions point approximately parallel to fracture zones which curve away from the direction of current plate motion in the old Pacific.

The results of the comparison between the anisotropic fast-axis directions and the paleo-spreading directions are shown in Figures 14 - 16 and should be contrasted with the comparison between the fast-axis directions and present plate motion directions seen in Figures 10 - 12. The contrast is that the worst agreement is at 150 sec period and agreement between the fast-axis directions and the paleo-spreading directions is best at shorter periods, particularly at 50 sec. Comparison of Figures 16b and 16d is telling. At 50 sec period, the agreement between the fast-axis directions and the paleo-spreading directions is nearly independent of lithospheric age, but the discrepancy grows strongly with age at 150 sec period. As period decreases below 50 sec, there is increasing sensitivity to anisotropy in the crust. We believe this is the reason why the maps at 25 sec (Fig. 14a) and below disagree with the paleo-spreading direction more than the intermediate period maps such as the one shown at 50 sec period (Fig. 14b).

4.3 Two-Layered Stratification of Azimuthal Anisotropy in the Uppermost Mantle

The results in sections 4.1 and 4.2 indicate that in the shallow lithosphere, anisotropic fast axis directions tend to align with the paleo-spreading direction. In the deeper lithosphere

and asthenosphere, the anisotropic fast axes are oriented more nearly along present day plate motions. We infer from this, therefore, that anisotropy in the cool uppermost mantle is controlled by conditions that prevailed at the time of formation of the lithosphere. Subsequent changes in mantle flow are not revealed by anisotropy in the shallowest mantle. In the warmer asthenosphere, however, anisotropy has re-oriented to conform to current conditions of flow that are revealed by present-day plate motion. This "two-layer" model of mantle anisotropy beneath the Pacific is presented in idealized form in Figure 17. Anisotropic fast axes are oriented parallel to current mantle flow in the deep lithosphere and asthenosphere, but are "frozen" or fixed in the lithosphere revealing the strain conditions active during the early evolution of the lithosphere.

An idea of the depth extent of the layer of fixed anisotropy can be obtained from Figure 18 in which the 2ψ azimuthal anisotropy maps on a grid of periods ranging from 20 to 150 sec were used to illustrate the period dependence of the azimuthal difference between the anisotropic fast axis and the plate motion directions along a great circle path from the Western Pacific to the East Pacific Rise. Because the depths sampled by surface waves increase with period, as shown in Figure 8, period can be used an an approximate proxy for depth. Figure 18 illustrates that large differences between the fast axis of azimuthal anisotropy and the direction of present-day plate motion set-on between $\sim$ 40 - 70 Ma and exist primarily at periods below about 80 sec. Because the sensitivity of 80 sec Rayleigh group speed peaks at about 80 km depth, the zone of fixed anisotropy probably does not extend deeper than about 100 km in the Western Pacific. This depth probably depends on lithospheric age and could vary regionally, but these issues are beyond the scope of the present work.

Another line of evidence supporting a two-layer model of anisotropy in the upper mantle beneath the Pacific results from a consideration of how the amplitude of anisotropy (eq. (4)) varies with period and lithospheric age. Figure 19 shows that at long periods there is a decrease in amplitude in the old Pacific relative to the amplitudes in the young Pacific. The amplitude of anisotropy on the 25 sec map does not decrease in the western Pacific and the biggest east-west discrepancy in amplitude comes at 100 sec period. The east-west discrepancy can result from destructive interference at periods sensitive to anisotropy in both layers. Thus, at 25 sec period where sensitivity is exclusively limited to the layer in which anisotropy is

frozen into the lithosphere, the strength of anisotropy does not decrease in the old Pacific. Similarly, at 150 sec which is dominantly (although not exclusively) sensitive to the deeper layer of anisotropy, the decrease in the strength of anisotropy with age will be weaker than at the intermediate periods of 50 sec and 100 sec. At 50 sec and 100 sec period, the east-west discrepancy is largest because the waves are strongly sensitive both to the fixed anisotropy of the upper lithosphere and the conformable anisotropy of the underlying asthenosphere.

This argument to explain the trend of the amplitude of azimuthal anisotropy with lithospheric age is purely qualitative and is intended only as a consistency check of the two-layer model of azimuthal anisotropy. There may be other plausible sources for this decrease in azimuthal anisotropy in the deep lithosphere to upper asthenosphere in the west Pacific. For example, the hypothesized change in the direction of plate motion at about 43 Ma (e.g., Lithgow-Bertelloni and Richards, 1998) could cause a decrease in the amplitude of anisotropy in the asthenosphere and lower lithosphere, where some fraction of the olivine crystals may have kept their original orientation after the plate changed directions. This potential change in plate motion, however, is contentious (e.g., Norton, 1994; Tarduno et al., 2003). The decrease in the amplitude of azimuthal anisotropy could also be evidence for a disruption in the deep lithosphere or asthenosphere of the central Pacific that could arise from thermal boundary layer instabilities (e.g., Ritzwoller et al., 2004) or multiple thermal plumes, but modeling needs to be performed in order to explain simultaneously the amplitude pattern, the fast axis directions, and the nature of the isotropic part of the model.

4.4 Water in the Uppermost Mantle

Jung and Karato (2001) show that when a large amount of water is introduced into olivine, the relation between the flow direction and the induced anisotropy changes. Our findings suggest that at large-scales across the Pacific, the relation between anisotropy and flow (present or at the time of lithospheric formation, depending on the depth) is, on average, rather simple. We take this as evidence that large amounts of water are not present in the uppermost mantle beneath most of the Pacific. This does not preclude the possibility that large amounts of water are locally present in the upper mantle, say due to enrichment of volatile content near subduction zones.

4.5 Potential Cause(s) of the Stratification of Anisotropy

There are two alternative hypotheses concerning the cause of the two layered stratification of anisotropy across the Pacific upper mantle, in which anisotropy is able to conform with current flow conditions in the asthenosphere and the deep lithosphere whereas shallow lithospheric anisotropy appears to be "frozen in" and aligns nearer to the paleo-spreading direction. The first hypothesis is that the stratification simply reflects temperature. The lower temperatures in the shallow lithosphere prohibit dislocation creep from occurring as fast as in the asthenosphere. Under this interpretation, anisotropy is frozen into the shallow lithosphere because temperatures are simply too low for dislocation creep to have reoriented crystal axes as plate motions have changed during the history of the Pacific lithosphere. The second hypothesis is somewhat more subtle. It asserts that anisotropy will form only near shear flows and, as the lithosphere grows, the upper reaches of shear flow deepens into the mantle. Under this interpretation, the reason why anisotropy is frozen into the shallow lithosphere is because the shear strains that can cause a change in anisotropy occur at greater depths as the plate ages.

It is likely that both temperature and the depth extend of shear flows play a role in the stratification of anisotropy in the Pacific. We favor later hypothesis, but detailed modeling will be needed to settle the question.

Appendix: On Diffraction Tomography in Anisotropic Media

Surface wave "diffraction tomography" (e.g., Ritzwoller et al., 2002) is based on a Born-approximation solution to the two-dimensional acoustic wave equation (e.g., Spetzler and Snieder, 2001) that provides a reasonable approximation for the propagation of a single-mode surface wave (Rayleigh or Love) in a slightly heterogeneous, isotropic medium. Within this approximation, travel time perturbations are estimated as surface integrals with two-dimensional sensitivity kernels, in contrast with the line integrals along rays that emerge in traditional ray theory. Finite frequency effects should also be accounted for when using surface-wave tomography to estimate travel times through an azimuthally anisotropic medium. We are not aware, however, of the existence of a theory that describes the anisotropic finite-frequency surface-wave sensitivity kernels. In the absence of a solid

theoretical foundation, we introduce anisotropic kernels by simple analogy with the isotropic theory. At the center of the analogy, however, is an ambiguity concerning the definition of the angle at the scatterer. We consider several alternative definitions for this angle and show that, irrespective of this choice, the principal features of azimuthal anisotropy estimated across the Pacific remain relatively unchanged.

Travel Time Through an Anisotropic Medium: Ray theory

Ray-theoretical travel time perturbations in an anisotropic medium can be written as an integral along the ray path p (e.g., Barmin et al, 2001):

$$\delta t^r = \int_p \frac{m(\mathbf{r})}{c_0} ds \tag{A1}$$

where c_0 is the reference phase or group speed and:

$$m(\mathbf{r}) = \sum_{k=0}^{4} \gamma_k(\psi(\mathbf{r})) m_k(\mathbf{r}) \tag{A2}$$

$$\begin{aligned}
\gamma_0(\psi) &= 1 & m_0(\mathbf{r}) &= (c_0 - c_I(\mathbf{r}))/c_I(\mathbf{r}) \\
\gamma_1(\psi) &= -\cos(2\psi) & m_1(\mathbf{r}) &= A_1(\mathbf{r}) c_0(\mathbf{r})/c_I^2(\mathbf{r}) \\
\gamma_2(\psi) &= -\sin(2\psi) & m_1(\mathbf{r}) &= A_2(\mathbf{r}) c_0(\mathbf{r})/c_I^2(\mathbf{r}) \\
\gamma_3(\psi) &= -\cos(4\psi) & m_1(\mathbf{r}) &= A_3(\mathbf{r}) c_0(\mathbf{r})/c_I^2(\mathbf{r}) \\
\gamma_4(\psi) &= -\sin(4\psi) & m_1(\mathbf{r}) &= A_4(\mathbf{r}) c_0(\mathbf{r})/c_I^2(\mathbf{r})
\end{aligned} \tag{A3}$$

using notation from equations (1)-(3). The $k = 0$ term corresponds to isotropic perturbations and the $k = 1, \ldots, 4$ terms describe the 2ψ and the 4ψ anisotropic effects. For convenience, we can rewrite the travel time perturbation as a sum of contributions from the isotropic and anisotropic parts:

$$\delta t^r = \delta t_I^r + \delta t_A^r \tag{A4}$$

$$\delta t_I^r = \int_p \frac{c_0 - c_I(\mathbf{r})}{c_0 c_I(\mathbf{r})} ds \tag{A5}$$

$$\delta t_A^r = \sum_{k=1}^{4} \int_p \frac{\gamma_k(\psi(\mathbf{r})) m_k(\mathbf{r})}{c_0} ds. \tag{A6}$$

Travel Time Through an Isotropic Medium: Diffraction Theory

In an isotropic medium, equation (A4) is reduced to equation (A5). In this case, the transition from ray theory to diffraction theory is achieved by substituting the linear integral along the path with a surface integral:

$$\delta t_I^d = \int_S K(\mathbf{r}) \frac{c_0 - c_I(\mathbf{r})}{c_0 c_I(\mathbf{r})} d\mathbf{r}^2 \tag{A7}$$

where $K(\mathbf{r})$ is the diffraction sensitivity kernel (e.g., Spetzler and Snieder, 2001; Ritzwoller et al., 2002) and $d\mathbf{r}^2$ is an area-element.

Travel Time Through an Anisotropic Medium: Diffraction Theory

To write diffraction-theory travel times in an anisotropic medium analogously with the isotropic case we replace the linear integrals along the ray with the surface integrals:

$$\delta t_A^d = \sum_{k=1}^{4} \int_S K(\mathbf{r}) \frac{\gamma_k(\psi(\mathbf{r})) m_k(\mathbf{r})}{c_0} d\mathbf{r}^2, \tag{A8}$$

where $K(\mathbf{r})$ is the same kernel as in the isotropic case. The principal problem with this ad-hoc definition of the anisotropic diffraction kernels is that the local propagation angle at the scatterer $\psi(\mathbf{r})$ and, consequently, the anisotropic kernels are not uniquely defined outside the great-circle connecting the source and the receiver. There are several alternative ways to define the angle at the scatterer, some of which are shown in Figure 20. The use of the angle ψ_1 (the direction of the scatterer from the source) or the angle ψ_2 (the direction of the scatterer from the receiver) has the disadvantage that reciprocity is not preserved. The use of angle ψ_3, the average of ψ_1 and ψ_2, will satisfy reciprocity as would the angle parallel to the great-circle (not shown in Fig. 20). We have considered three versions of the diffraction theory through an anisotropic medium based on sensitivity kernels that use angles ψ_1, ψ_2, and ψ_3. The respective kernels, $K_A^{d1}(\mathbf{r})$, $K_A^{d2}(\mathbf{r})$, and $K_A^{d3}(\mathbf{r})$, will generate three different travel times through the same azimuthally anisotropic model: δt_A^{d1}, δt_A^{d2}, and δt_A^{d3}. We note that these three angles differ from each other most appreciably away from the middle of the Fresnel zone; i.e., near the source and receiver. Therefore, the theories deviate most and are most uncertain near sources and receivers.

Azimuthal Anisotropy Estimated with Diffraction Theory and Ray Theory

We assume that none of these theories governing the effect of diffraction through an anisotropic medium is right, but attempt to use them to quantify the expected magnitude of the effect of diffraction on surface waves propagating in an anisotropic medium. In all of the inversions, we used diffraction theory for the isotropic part of the model but different theories (ray and diffraction) for the anisotropic part of the model. The ray theoretic results, therefore, refer to the use of diffraction theory is used for the isotropic part of the model and ray theory for the anisotropic part. The diffraction theoretic results use standard diffraction theory for the isotropic part (Ritzwoller et al., 2002) but one of the three variants of diffraction theory for the anisotropic part of the model.

We find, first, that the azimuthal anisotropy maps estimated with the diffraction theories based on kernels $K_A^{d1}(\mathbf{r})$, $K_A^{d2}(\mathbf{r})$, and $K_A^{d3}(\mathbf{r})$ are more similar to one another than any of them are to the anisotropy estimated using ray theory. The effect of incorporating diffraction, therefore, can be illustrated with the anisotropy maps that emerge from just one of the three variants of the theory. Second, Figure 21 shows that for the 50 sec Rayleigh wave group speed with our choice of smoothing and damping parameters, the large-scale pattern of 2ψ azimuthal anisotropy across Pacific is not strongly different from that which emerges from ray theory. The exception occurs in the Central Pacific (Fig. 21c) where the amplitude of anisotropy is small. There is, however, a much more significant difference in continents. There are similar results at other periods. Finally, the difference between the theories is also more prominent if we damp the anisotropic maps less.

The results shown in Figure 21 can be partially understood in light of the fact that the wave paths across most of the Pacific tend to be long. The biggest differences among the diffraction theories themselves and between them and ray theory occur near sources and receivers, which are relatively rare across the Pacific. It is near source locations (i.e., plate boundaries generally), near receiver locations (i.e., continents generally), and for smaller scale structure that the effects of diffraction through the anisotropic medium become important. This is a cautionary note for the estimation of azimuthal anisotropy in continental areas, in particular, but across the Pacific the large-scale results are robust relative to the theory chosen.

Acknowledgement

This work benefited from discussions with Thorsten Becker, Martha Savage, Roel Snieder, and Shi-Jie Zhong. We gratefully acknowledge the staffs at the IRIS-DMC and the GEOFON and GEOSCOPE data centers for providing most of the waveform data on which results are based. We thank Jeannot Trampert at Utrecht University and Michael Antolik, Adam Dziewonski, and Goran Ekström at Harvard University for providing phase speed measurements. As always, we are grateful to Mikhail Barmin for assistance with the surface wave tomography. All maps were generated with the Generic Mapping Tools (GMT) data processing and display package (Wessel and Smith, 1991, 1995). This work was supported by grants from the US National Science Foundation (OPP-0125848, OPP-0136103, EAR-0409217).

References

Aki, K. and K. Kaminuma, Phase velocities in Japan. Part I. Love waves from the Aleutian shock of March 9, 1957, *Bull. Earthq. Res. Inst., 41*, 243-259, 1963.

Babuska, V. & Cara, M., *Seismic Anisotropy in the Earth*, Kluwer, Dordrecht, 1991.

Barmin, M.P., Levshin, A.L., & Ritzwoller, M.H., A fast and reliable method for surface wave tomography, *Pure appl. Geophys.*, **158**, 1351-1375, 2001.

Becker, T.W., Kellogg, J.B., Ekström, G., & O'Connell, R.J., Comparison of azimuthal seismic anisotropy from surface waves and finite-strain from global mantle-circulation models, *Geophys. J. Int.*, **155**, 696-714, 2003.

Blackman, D.K. and J.-M. Kendall, Seismic anisotropy of the upper mantle: 2. Predictions for current plate boundary flow models, *Geochemistry, Geophysics, and Geosystems, 3* (2001GC000247), 2002.

Blackman, D.K. H.-R. Wenk, and J.-M. Kendall, Seismic anisotropy of the upper mantle: 1. Factors that affect mineral texture and effective elastic properties, *Geochemistry, Geophysics, and Geosystems, 3* (2001GC000248), 2002.

Buttles, J. and P. Olson, A laboratory model of subduction zone anisotropy,*Earth Planet. Sci. Lett., 164*, 245-262, 1998.

Chastel, Y.B., P.R. Dawson, H.-R. Wenk, and K. Bennett, Anisotropic convection with implications for the upper mantle, *J. Geophys. Res., 98*, 17757-17771, 1993.

Dziewonski, A.M. and D.L. Anderson, Preliminary Reference Earth Model, *Phys. Earth Planet. Inter., 25*, 297-356, 1981.

Ekström, G., Mapping the lithosphere and asthenosphere with surface waves: Lateral structure and anisotropy, in M.A. Richards, R. Gordon, and R. van der Hilst (eds.), The History of Global Plate Motions, Am. Geophys. Un., Washington, D.C., 211-238, 2000.

Ekström, G. and A.M Dziewonski, The unique anisotropy of the Pacific mantle, *Nature, 394*, 168-172, 1998.

Forsyth, D.W., The early structural evolution and anisotropy of the oceanic upper mantle, *Geophys. J. R. Astr. Soc., 43*, 103-162, 1975.

Gaboret, C., A.M. Forte, and J.-P. Montagner, The unique dynamics of the Pacific hemisphere mantle and its signature on seismic anisotropy, *Earth Planet. Sci. Lett., 208*, 219-233, 2003.

Griot, D.A., Montagner, J.-P., and Tapponier, P., Surface wave phase velocity tomography and azimuthal anisotropy in Central Asia, *J. geophys. Res.*, **103**, 21215-21232, 1998.

Gripp, A.E. & Gordon, R.G., Young tracks of hotspots and current plate velocities, *Geophys. J. Int., 150*, 321-361, 2002.

Hall, C.E., K.M. Fischer, and E.M Parmentier, The influence of plate motions on three-dimensional back arc mantle flow and shear wave splitting, *J. Geophys. Res., 105*, 28009-28033, 2000.

Hess, H.H., Seismic anisotropy of the uppermost mantle under oceans, *Nature, 203*, 629-631, 1964.

Jung, H. and S. Karato, Water-induced fabric transitions in olivine, *Science, 293*, 1460-1463, 2001.

Kaminski, E. and N. Ribe, A kinematic model for the recrystallization and texture development in olivine polycrystals, *Earth Planet. Sci. Lett., 189*, 253-267, 2001.

Larsen, E.W.F, J. Tromp, and G. Ekström, Effects of slight anisotropy on surface waves, *Geophys. J. Int., 132*, 654-666, 1998.

Levin, V., W. Menke, and J. Park, Shear wave splitting in the Appalachians and the Urals: A case for multilayer anisotropy, *J. Geophys. Res., 104*, 17975-17993, 1999.

Levshin, A.L., M.P. Barmin, M.H. Ritzwoller, and J. Trampert, Using both minor and major arc data for global surface wave diffraction tomography, submitted to *Phys. Earth Planet. Ints.*, 2004.

Lithgow-Bertelloni, C., and M.A. Richards, The dynamics of Cenozoic and Mesozoic plate motions, *Revs. Geophys., 36*, 27-78, 1998.

McEvilly, T.V., Central US crust – upper mantle structure from Love and Rayleigh wave phase velocity inversion, *Bull. Seism. Soc. Am., 54*, 1997-2015, 1964.

McKenzie, D.P., Finite deformations during fluid flow, *Geophys. J. R. Astr. Soc., 58*, 689-715, 1979.

Montagner, J.-P., Where can seismic anisotropy be detected in the Earth's mantle? In boundary layers ..., *Pure appl. Geophys., 151*, 223-256, 1998.

Montagner, J.-P. and T. Tanimoto, Global upper mantle tomography of seismic velocities and anisotropies, *J. geophys. Res., 96*, 20337-20351, 1991.

Morris, G.B., R.W. Raitt, and G.G. Shor, Velocity anisotropy and delay-time maps of the mantle near Hawaii, *J. Geophys. Res., 74*, 4300-4316, 1969.

Mueller, R.D., Roest, W.R., Royer, J.-Y., Gahagan, L.M., & Sclater, J.G., Digital isochrons of the world's ocean floor, *J. Geophys. Res., 102*, 3211-3214, 1997.

Nataf, H.-C., I. Nakanishi, and D.L. Anderson, Anisotropy and shear velocity heterogeneity in the upper mantle, *Geophys. Res. Lett., 11*, 109-112, 1984.

Nishimura, C.E. and D.W. Forsyth, The anisotropic structure in the upper mantle of the Pacific, *Geophys. J., 96*, 203-229, 1989.

Norton, I.O., Plate motions in the North Pacific: The 43 Ma non-event, *Tectonics, 14*, 1080-1094, 1995.

Peyton, V., V. Levin, J. Park, M. Brandon, J. Lees, E. Gordeev, and A. Ozerov, Mantle flow at a slab edge: Seismic anisotropy in the Kamchatka region, *Geophys. Res. Lett., 28(2)*, 379-382, 2001.

Raitt, R.W., G.G. Shor, T.J.G. Francis, and G.B. Morris, Anisotropy of the Pacific upper mantle, *J. Geophys. Res., 74*, 3095-3109, 1969.

Regan, J. and D.L. Anderson, Anisotropic models of the upper mantle, *Phys. Earth Planet. Inter., 35*, 227-263, 1984.

Ribe, N.M., Seismic anisotropy and mantle flow, *J. Geophys. Res., 94*, 4213-4223, 1989.

Ribe, N.M., On the relation between seismic anisotropy and finite strain, *J. Geophys. Res., 97*, 8737-8747, 1992.

Ribe, N.M. and Y. Yu, A theory for plastic-deformation and textural evolution of olivine polycrystals, *J. Geophys. Res., 96*, 8325-8335, 1991.

Ritzwoller, M.H. & Levshin, A.L., Eurasian surface wave tomography: group velocities, *Geophys. J. Int., 134*, 315-328, 1998.

Ritzwoller, M.H., Shapiro, N.M., Barmin, M.P., & Levshin, A.L., Global surface wave diffraction tomography, *J. geophys. Res., 107(B12)*, 2335, doi:10.1029/2002JB001777. 2002.

Ritzwoller, M.H., N.M. Shapiro, and S. Zhong, Cooling history of the Pacific lithosphere, *Earth Planet. Sci. Letts.*, submitted, 2004.

Romanowicz, B. and R. Snieder, A new formalism for the effect of lateral heterogeneity on normal modes and surface waves, II. General anisotropic perturbations, *Geophys. J. R. Astr. Soc., 93*, 91-99, 1988.

Russo, R.M. and P.G. Silver, Trench-parallel flow beneath the Nazca plate from seismic anisotropy, *Science, 263*, 1105-1111, 1994.

Savage, M.K., Seismic anisotropy and mantle deformation: What have we learned from shear wave splitting?, *Rev. Geophys., 37*, 65-106, 1999.

Savage, M.K. and P.G. Silver, The interpretation of shear-wave splitting parameters in the presence of two anisotropic layers, *Geophys. J. Int., 119*, 949-963, 1994.

Shapiro, N.M. & Ritzwoller, Monte-Carlo inversion for a global shear velocity model of the crust and upper mantle, *Geophys. J. Int., 151*, 88-105, 2002.

Shapiro, N.M., M.H. Ritzwoller, P. Molnar, and V. Levin, Thinning and flow of Tibetan crust constrained by seismic anisotropy. *Science*, in press, 2004.

Shearer, P.M. and J.A. Orcutt, Compressional and shear wave anisotropy in the oceanic lithosphere – the Ngendei seismic refraction experiment, *Geophys. J.R. Astr. Soc., 87*, 967-1003, 1986.

Silver, P.G. and W.E. Holt, The mantle flow field beneath western North America, *Science, 295*, 1054-1057, 2002.

Smith, M.L. & Dahlen, F.A., The azimuthal dependence of Love and Rayleigh waves propagation in a slightly anisotropic medium, *J. geophys. Res., 78*, 3321-3333, 1973.

Spetzler, J. and R. Snieder, The effects of small-scale heterogeneity on the arrival time of waves, *Geophys. J. Int., 145*, 786-796, 2001.

Tanimoto, T. and D.L. Anderson, Mapping convection in the mantle, *Geophys. Res. Lett, 11*, 287-290, 1984

Tarduno, J.A., R.A. Duncan, D.W. Scholl, R.D. Cottrell, B. Steinberger, T. Thordarson, B.C. Kerr, C.R. Neal, F.A. Frey, M. Torii, C. Carvallo, The Emperor Seamounts: Southward motion of the Hawaiian hotspot plume in earth's mantle, *Science, 301*, 1064-1069, 2003

Tommasi, A., Forward modeling of the development of seismic anisotropy in the upper mantle, *Earth Planet. Sci. Lett., 160*, 1-13, 1998.

Trampert, J. & Woodhouse, J.H., Global anisotropic phase velocity maps for fundamental mode surface waves between 40 and 150 s, *Geophys. J. Int., 154*, 154-165, 2003.

Vinnik, L., D. Peregoudov, L. Makeyeva, S. Oreshin, and S. Roecker, Towards 3-D fabric in the continental lithosphere and asthenosphere: The Tien Shan, *Geophys. Res. Letts., 29(16)*, Art. No. 1791, 2002.

Wessel, P and W. H. F. Smith, Free software helps map and display data, *Eos Trans. Amer. Geophys. Un., 72*, 441, 1991.

Wessel, P., and W.H.F. Smith, New version of the Generic Mapping Tools released, *Eos Trans. Amer. Geophys. Un., 76*, 329, 1995.

Wolfe, C.J. and S.C. Solomon, Shear-wave splitting and implications for mantle flow beneath the MELT region of the East Pacific rise, *Science, 280*, 1230-1232, 1998.

Zhang, S. and S.-I. Karato, Lattice preferred orientation of olivine aggregates deformed in simple shear, *Nature, 375*, 774-777, 1995.

Table 1. Peak coherence across the Pacific between Rayleigh wave group speed maps at the indicated periods.

	25 sec	50 sec	100 sec	150 sec
25 sec	1.00	0.62	0.56	0.53
50 sec	0.62	1.00	0.70	0.59
100 sec	0.56	0.70	1.00	0.82
150 sec	0.53	0.59	0.82	1.00

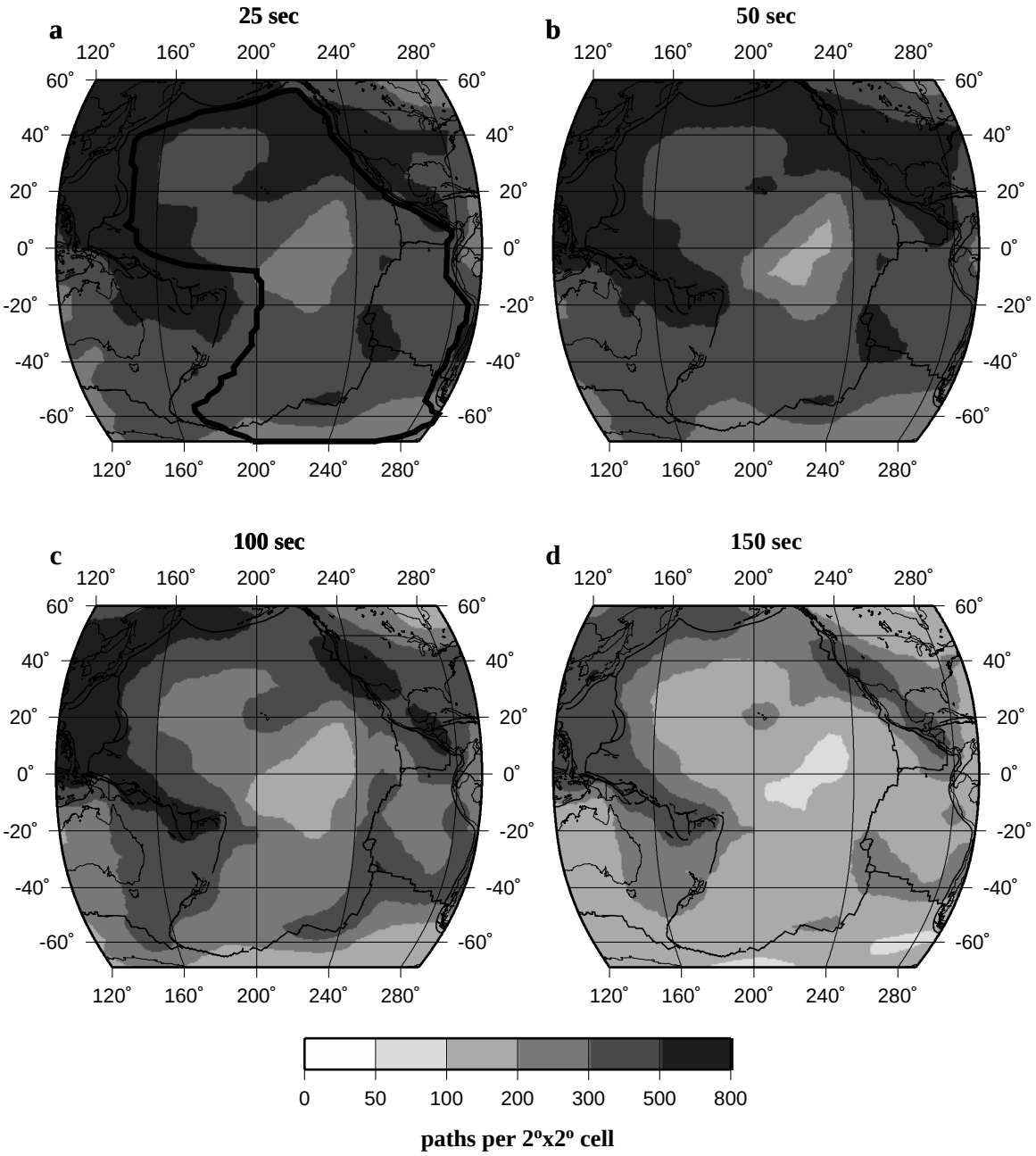

Figure 1. Path density for Rayleigh wave group velocities at the periods indicated. Path density is defined as the number of measurement paths crossing each $2^{\circ} \times 2^{\circ}$ cell (~50,000 km^2). In (a), the thick contour defines the area that we refer to as the "Pacific".

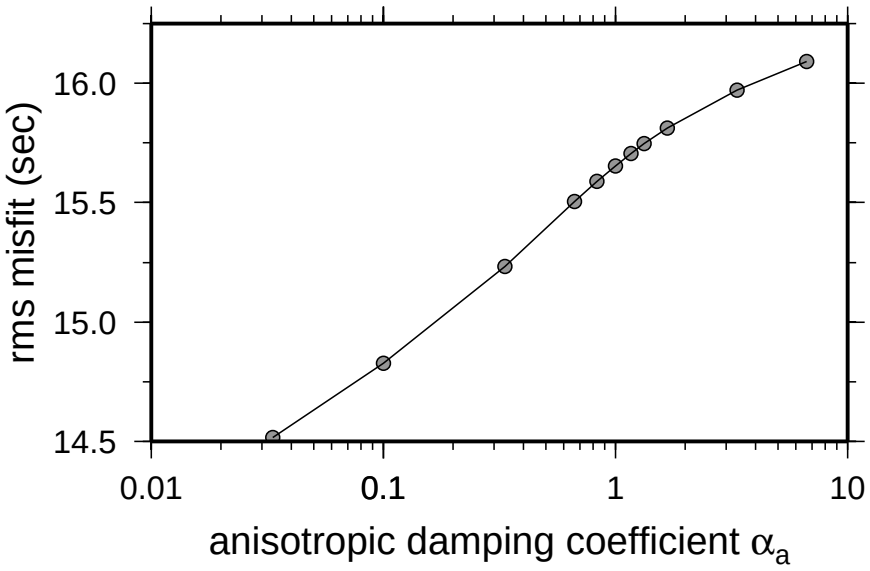

Figure 2. Misfit plotted versus a broad-range of values for the anisotropy damping parameter α_a for the 50 sec Rayleigh wave group speed. Misfit is defined as the rms-difference between the measured surface wave travel times and the travel times predicted by the estimated model, in seconds.

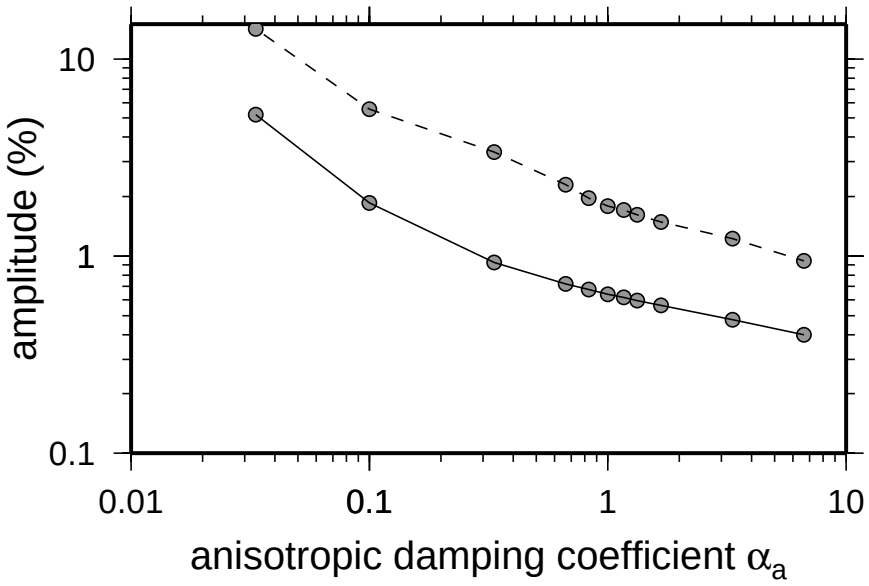

Figure 3. Amplitude of azimuthal anisotropy for the 50 sec Rayleigh wave group speed (eq. (4)) plotted versus a broad-range of values for the anisotropy damping parameter α_a. The solid line is the average across the Pacific and the dashed line is the maximum amplitude of anisotropy in the Pacific. There is, on average, about a factor of 3 between the average and maximum values.

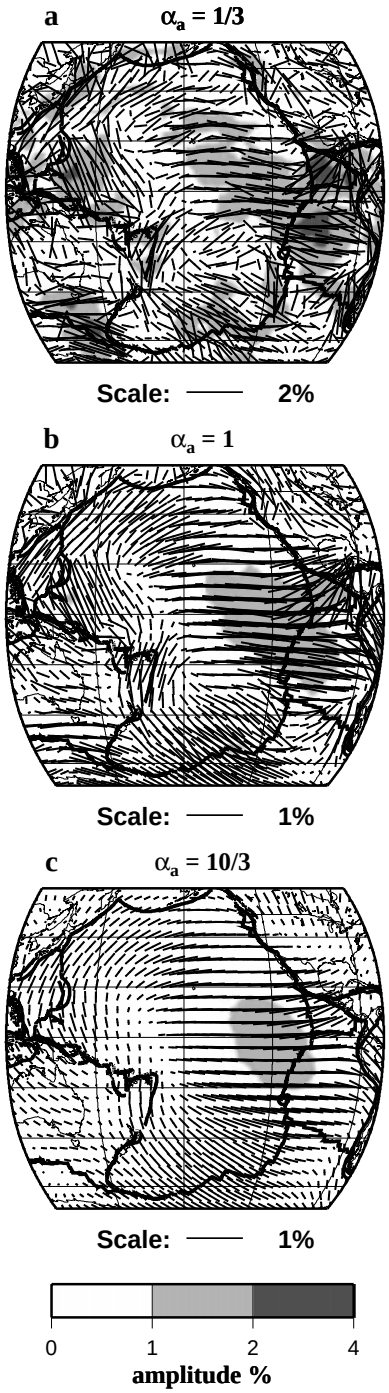

Figure 4. The 2ψ component of azimuthal anisotropy for 50 sec Rayleigh wave group speed estimated using three different values of the anisotropy damping parameter α_a: 1/3, 1, 10/3. Line segments show fast axis direction with the length proportional to the percent deviation from the reference velocity. Amplitudes, defined by equation (4), are shown with grey-shading.

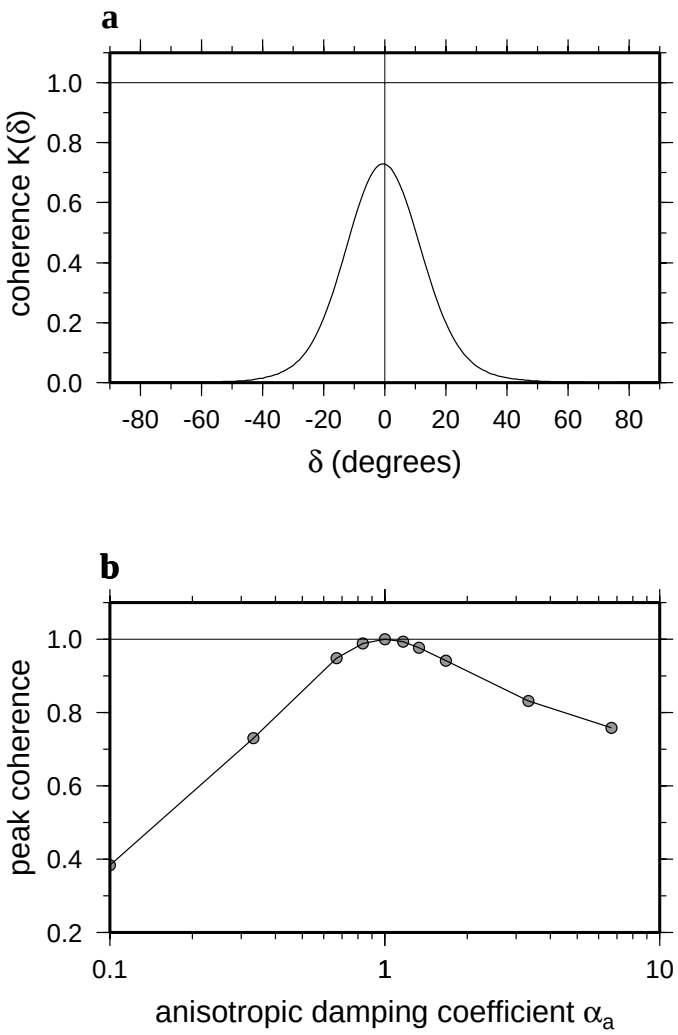

Figure 5. Spatial coherence (eq. (5)) across the Pacific of the Rayleigh wave group speed azimuthal anisotropy at 50 sec period for different values of the anisotropic damping parameter α_a. (a) Coherence between anisotropy estimated with $\alpha_a = 1$ and $\alpha_a = 1/3$. (b) Peak coherence between anisotropy estimated with $\alpha_a = 1$ and a broad range of different $\alpha_a = 1$. Peak coherence is the maximum value of coherence, approximately equal to the y-intercept on plots such as those in (a).

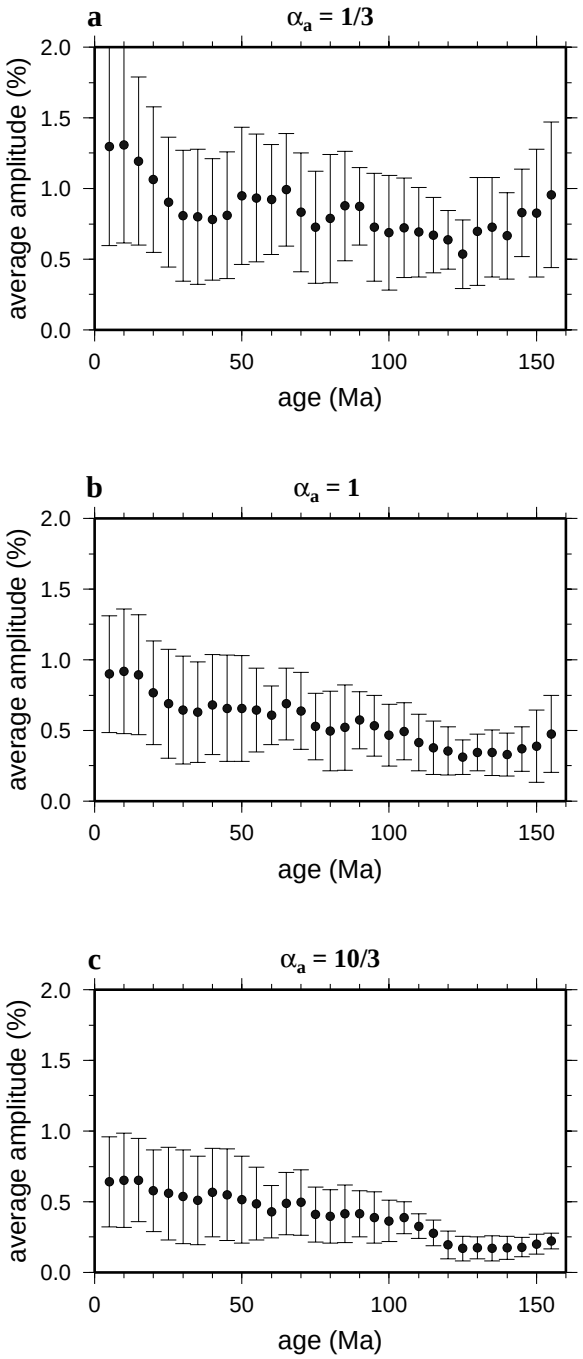

Figure 6. Amplitude of azimuthal anisotropy (eq. (4)) for the 50 sec Rayleigh wave group speed averaged across the Pacific and plotted versus lithospheric age (Mueller et al., 1997) for three different values of the anisotropy damping parameter: $\alpha_a = 1/3,\ 1,\ 10/3$. The "error bars" represent the standard deviation of the amplitudes within each age bin and the black dots are the means.

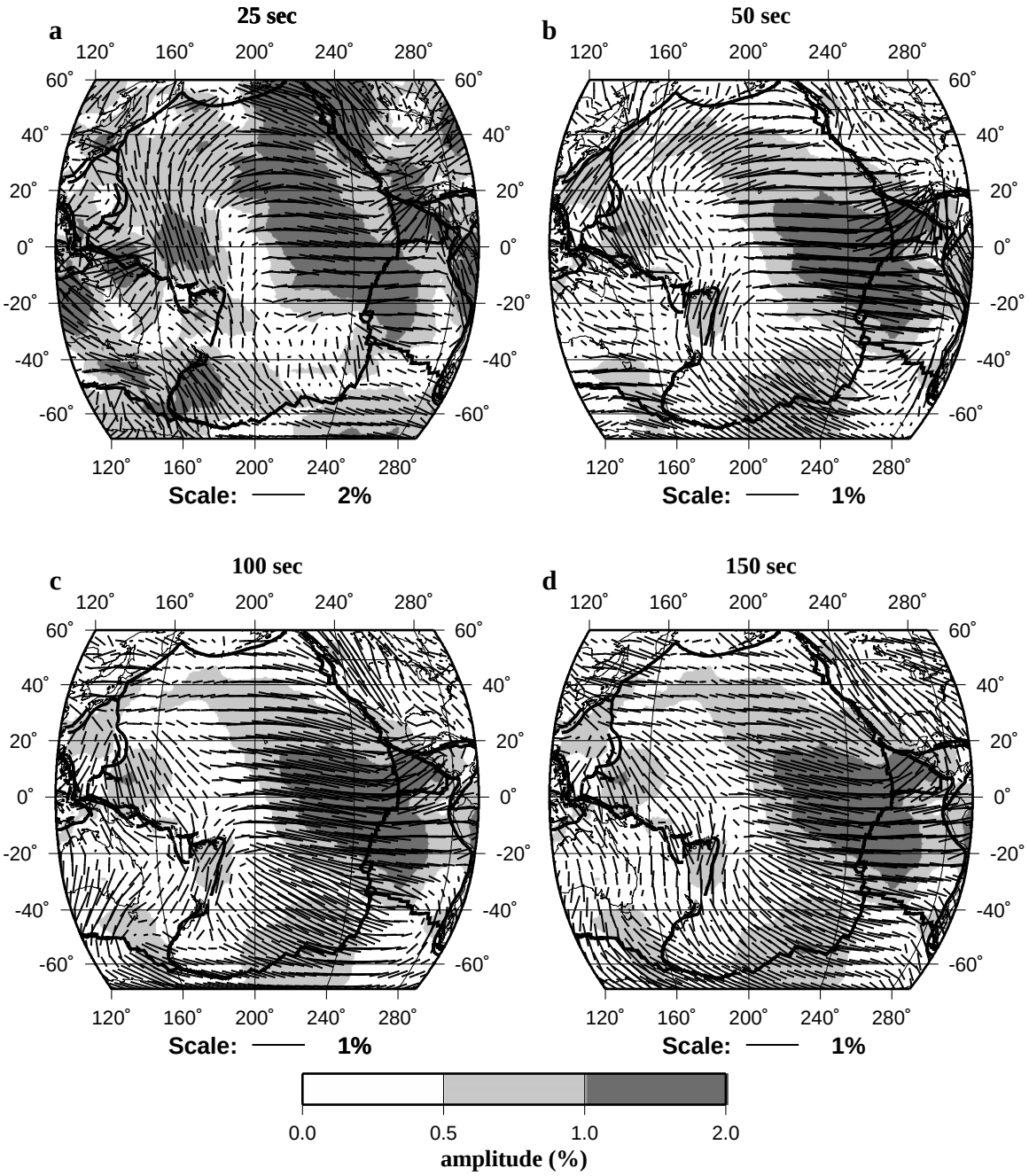

Figure 7. The 2ψ component of azimuthal anisotropy for Rayleigh wave group velocities across the Pacific. ($\sigma_i = 300$ km, $\alpha_i = 4/3$, $\sigma_a = 10^3$ km, $\alpha_a = 1$.) Line segments are the fast axis directions whose length is proportional to the amplitude of anisotropy (eq. (4))) presented as a percent deviation from a reference velocity. Amplitudes, defined by equation (4), are shown with grey-shading as in Figure 4.

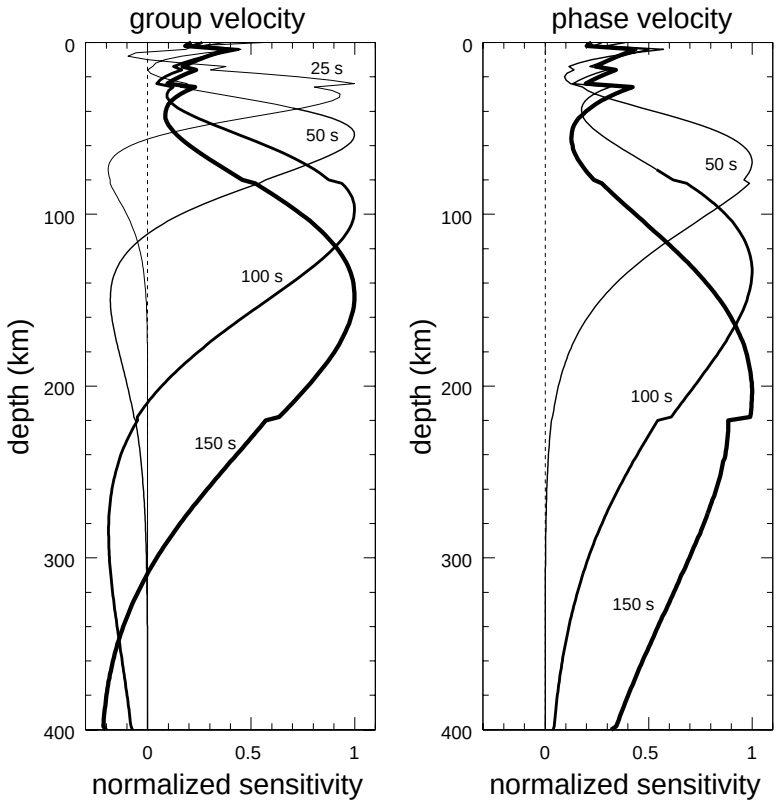

Figure 8. Sensitivity kernels for fundamental mode Rayleigh waves. (LEFT) Group velocity sensitivity kernels at 25 sec, 50 sec, 100 sec, and 150 sec periods. (RIGHT) Phase velocity sensitivity kernels at 50 sec, 100 sec, and 150 sec periods. The kernels are normalized, have units of inverse length, and are defined as $\partial c/\partial v_s$ at a constant frequency, where c is group or phase speed, and v_s is shear wave speed.

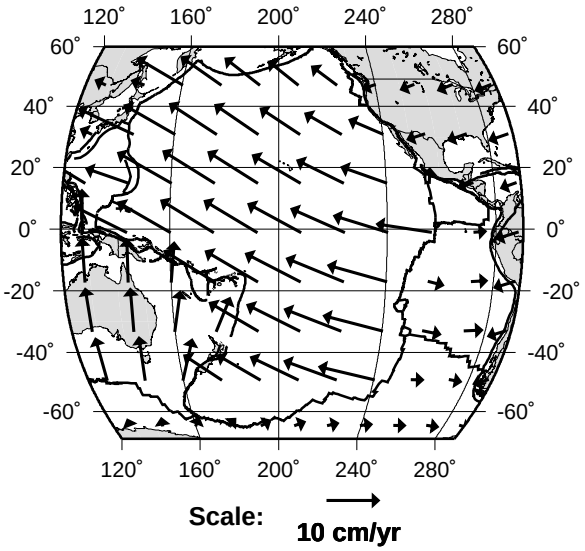

Figure 9. (a) Present-day plate motions defined in the hot-spot frame using the HS3-NUVEL-1A model [Gripp & Gordon, 2002].

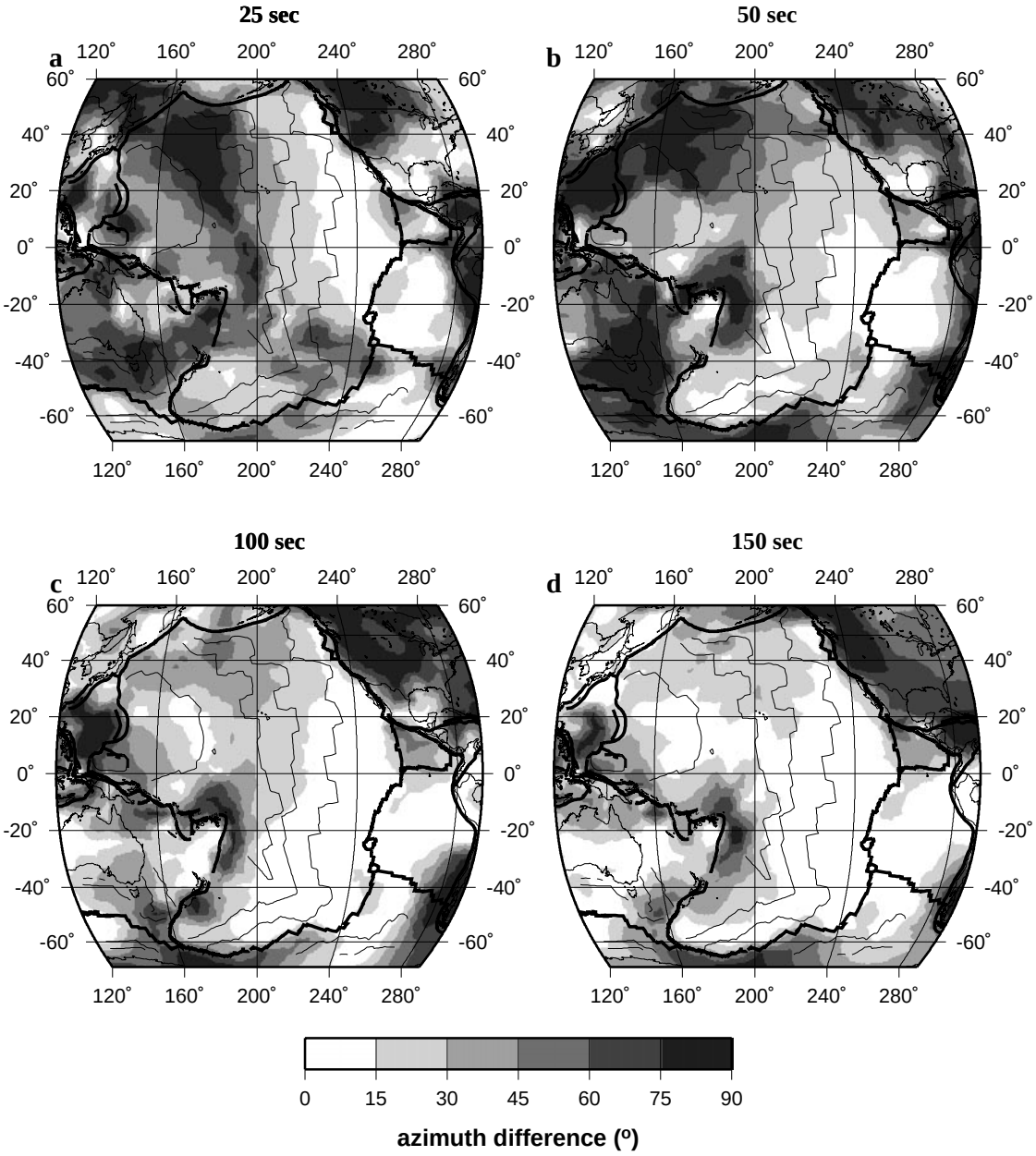

Figure 10. Difference in azimuth between the 2ψ component of azimuthal anisotropy (Fig. 7) and present-day plate motion (Fig. 9). In the young Pacific, the fast axes at all periods lie approximately parallel to plate motion except in the southern Pacific at 25 sec and in the Antarctic Plate. Even in the old Pacific the fast axes at 150 sec lie approximately parallel to plate motion. At shorter periods, however, fast axes increasingly diverge from the direction of plate motion. Isochrons of lithospheric age (Mueller et al., 1997) in 35 Ma increments are plotted for reference.

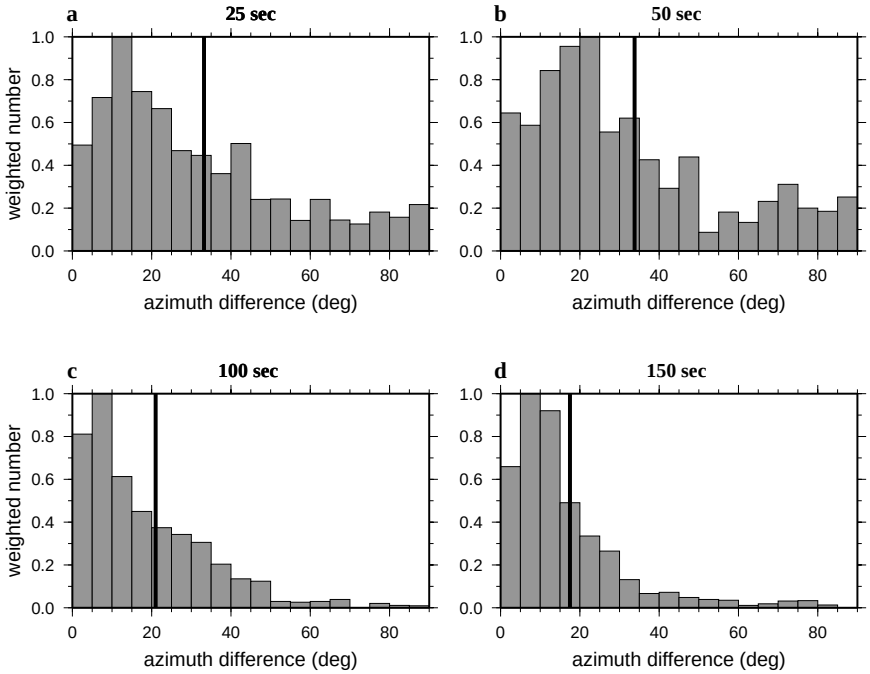

Figure 11. Normalized histograms of the difference in azimuth between the 2ψ fast axis directions and present-day plate motions for Rayleigh wave group speed at the indicated periods. The vertical line in each panel shows the weighted mean of the difference across the Pacific.

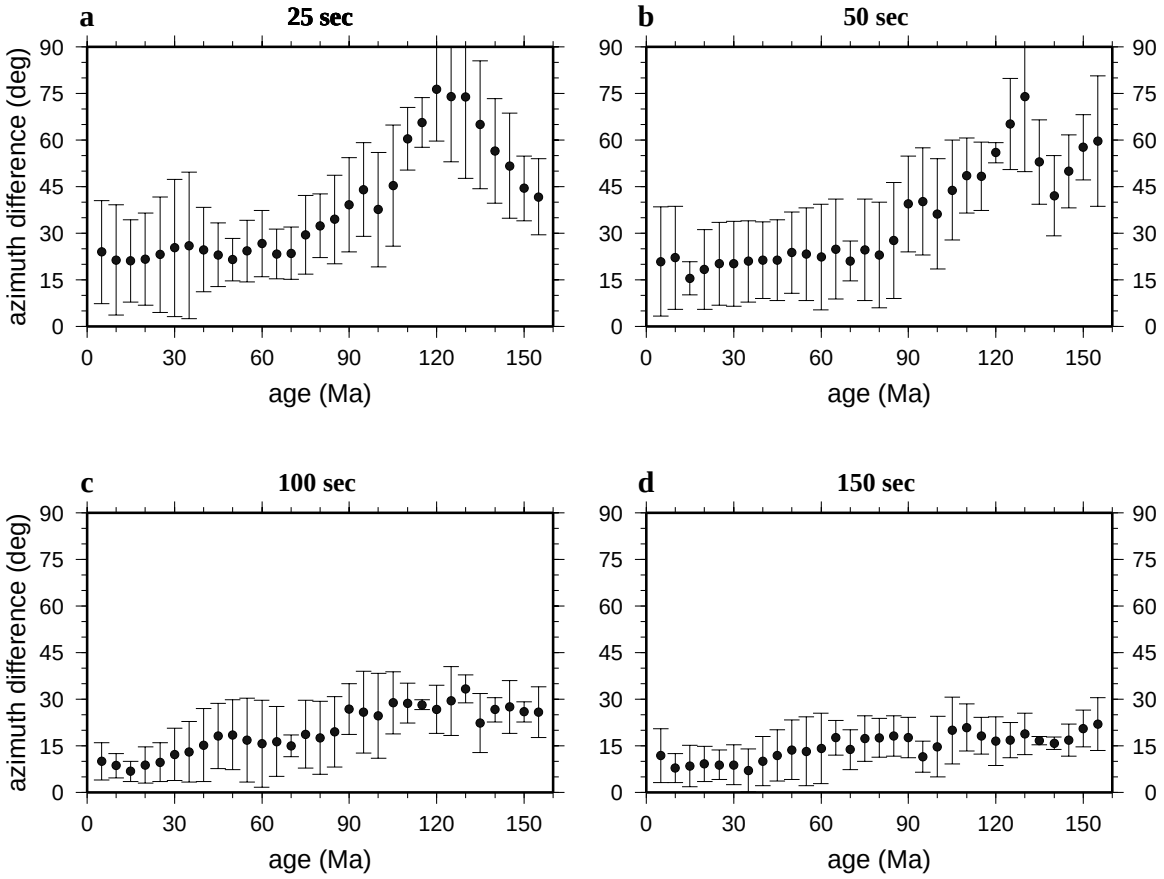

Figure 12. Difference in azimuth between anisotropic fast axis directions and the directions of plate motion plotted versus lithospheric age of the Pacific. The "error bars" are defined as in Figure 6. At young ages the fast axes at all periods align approximately parallel to plate motion. At old ages, the fast axes at long periods (c,d) tend to align parallel to plate motion, but for short periods (a,b) the fast axes diverge from plate motion directions. Each datum is weighted as in Figure 11.

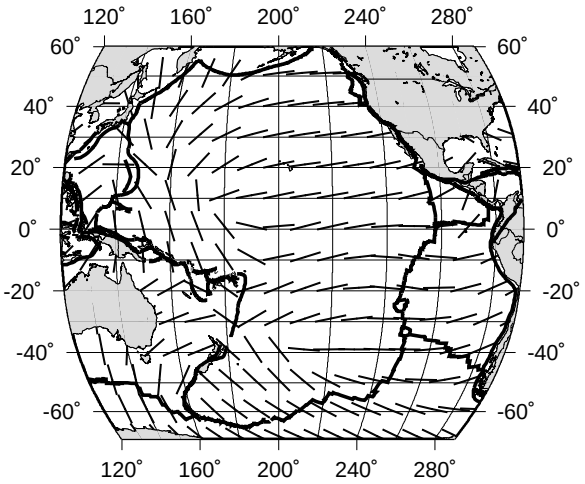

Figure 13. Estimated paleo-spreading directions computed from the gradient of lithospheric age (Mueller et al., 1997).

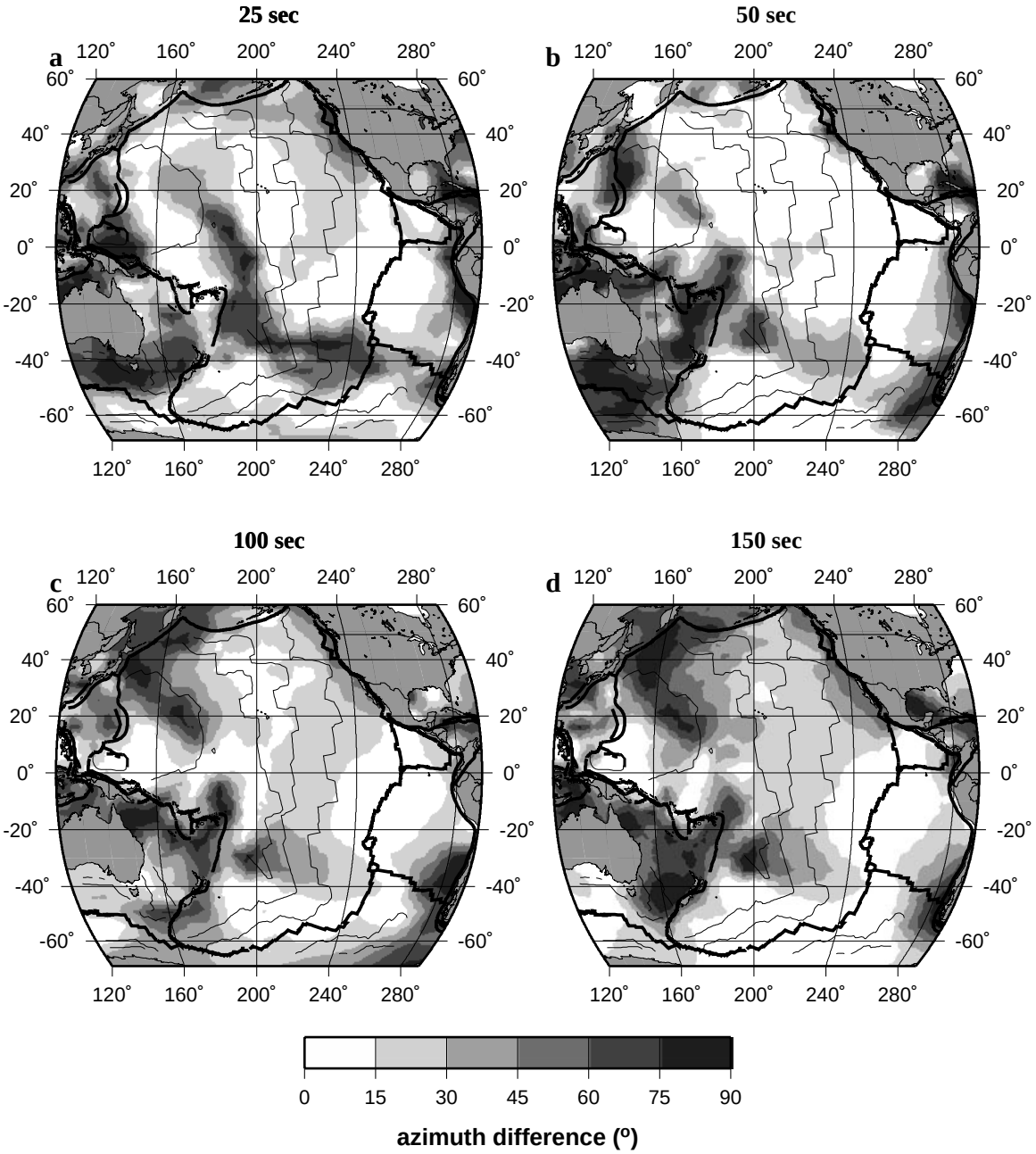

Figure 14. Same as Fig. 10, but this is the difference in azimuth between the 2ψ component of azimuthal anisotropy and the paleo-spreading direction. Agreement is best at 50 sec period and degrades as period increases.

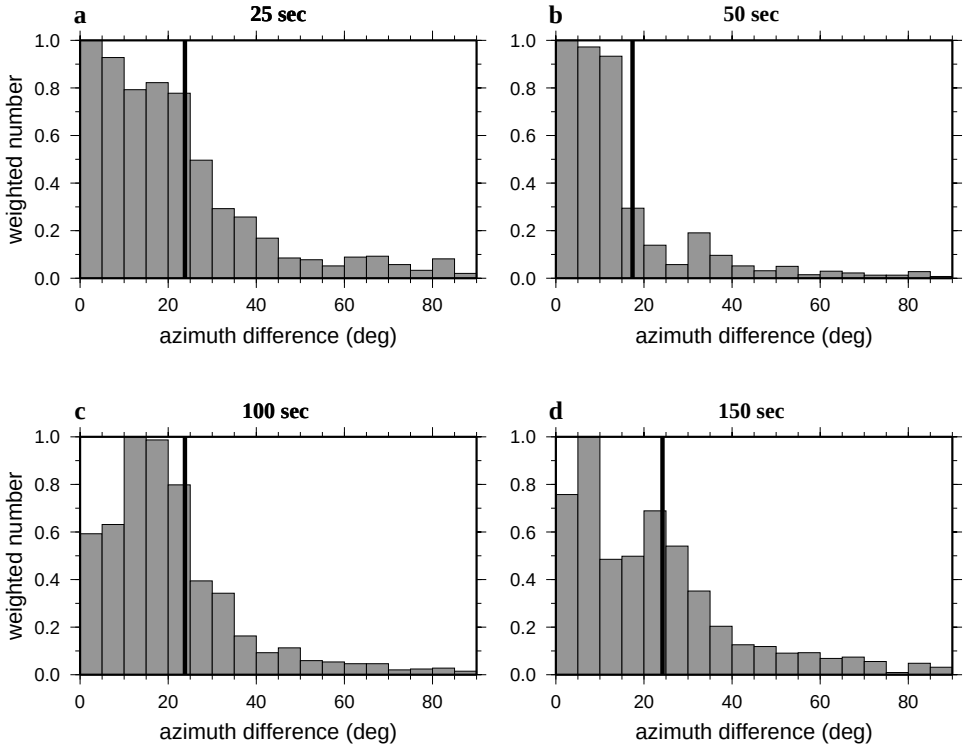

Figure 15. Same as Fig. 11, but these are histograms of differences in azimuth between the 2ψ component of azimuthal anisotropy and the paleo-spreading direction.

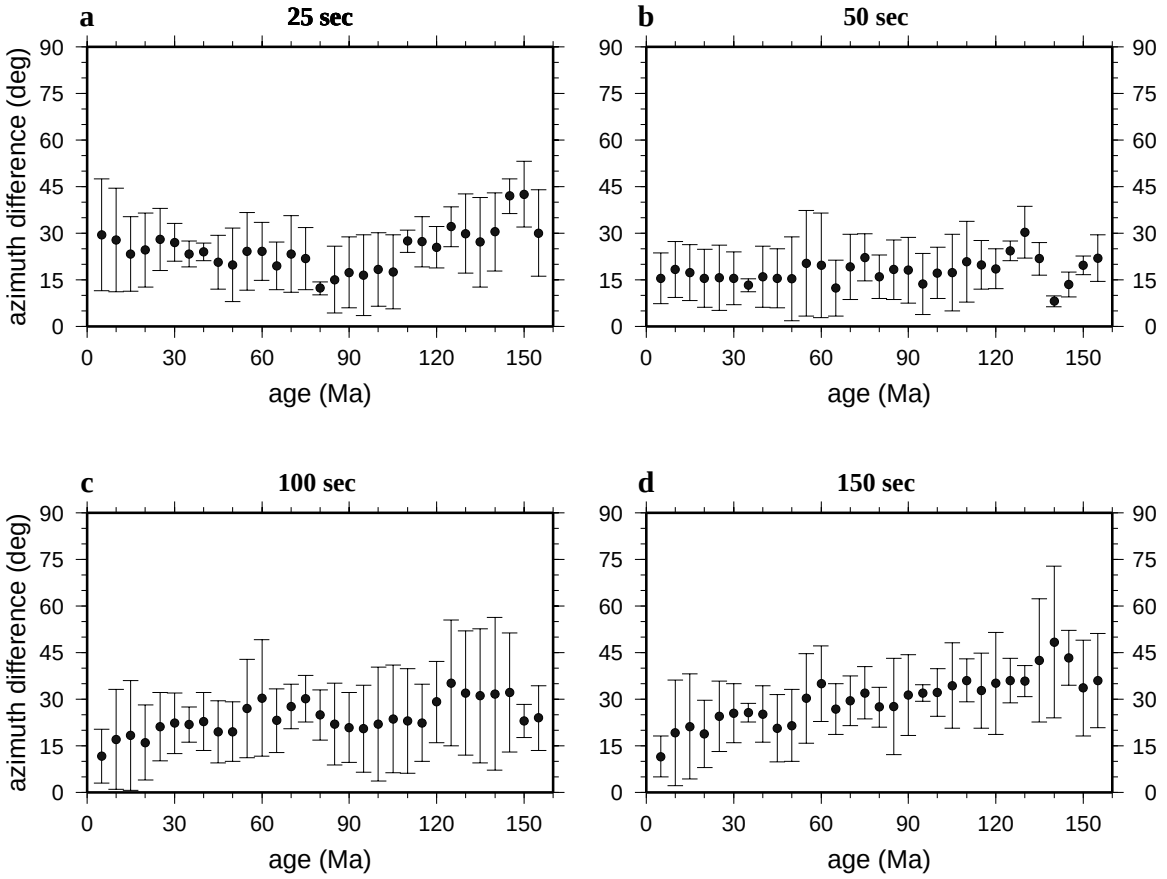

Figure 16. Same as Figure 12, but this is the difference between anisotropic fast axis directions and paleo-spreading directions. At young ages the fast axes approximately align parallel to the paleo-spreading directions. At old ages, the fast axes at short periods (a,b) align nearer to the paleo-spreading directions better than the fast axes for long periods (c,d). Each data point is weighted in the same manner as in Figure 11.

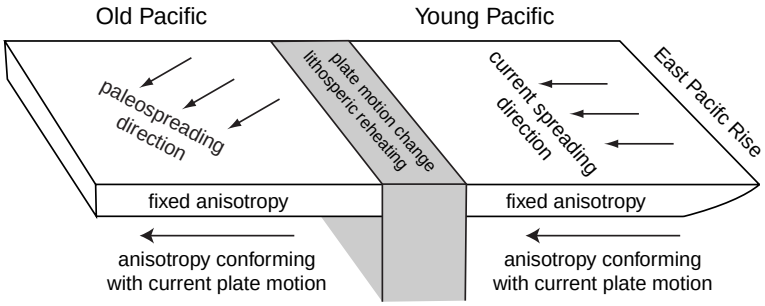

Figure 17. Two layer stratification of the average structure of azimuthal anisotropy in the Pacific upper mantle. In the asthenosphere and deep lithosphere, azimuthal anisotropy is able to conform to contemporary conditions and aligns approximately parallel to present-day plate motions. In the shallow lithosphere, the fast axes are fixed and align approximately parallel to the direction of spreading at the time of lithospheric formation.

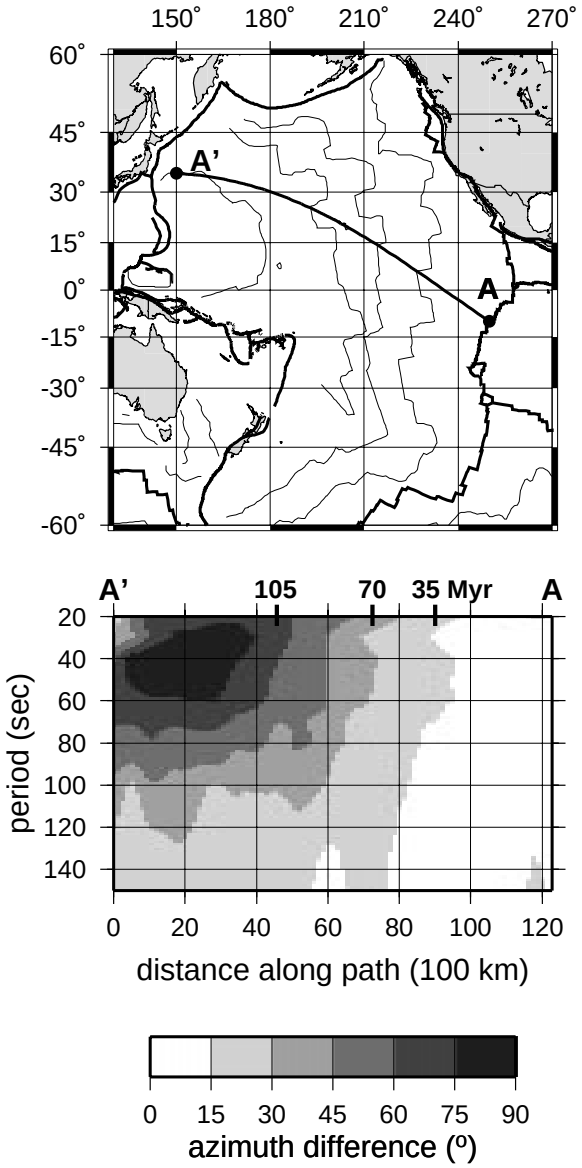

Figure 18. The period dependence (bottom) of the difference in azimuth between anisotropic fast axis directions and present-day plate motions along a great circle path across the Pacific (top). Because the period of the Rayleigh wave is an approximate proxy for depth of sensitivity (e.g., Fig. 8), this gives an idea of the depth variation of the fast axis directions relative to plate motions.

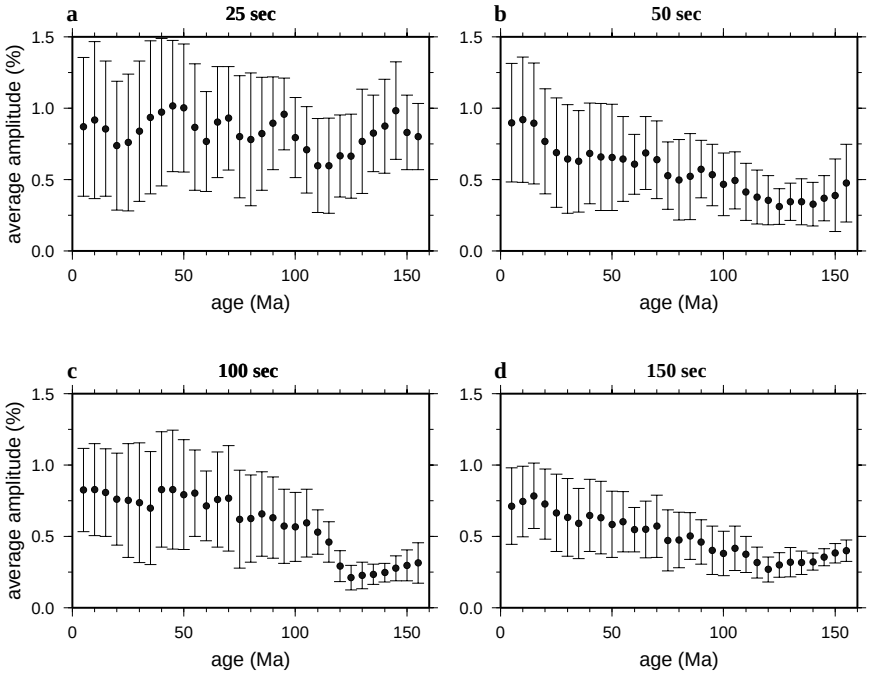

Figure 19. The amplitude of azimuthal anisotropy (eq. (4)) as a function of period and lithospheric age. At intermediate and long periods (50 - 150 sec), amplitudes decrease systematically with lithospheric age. At short periods (25 sec), amplitudes do not display this trend.

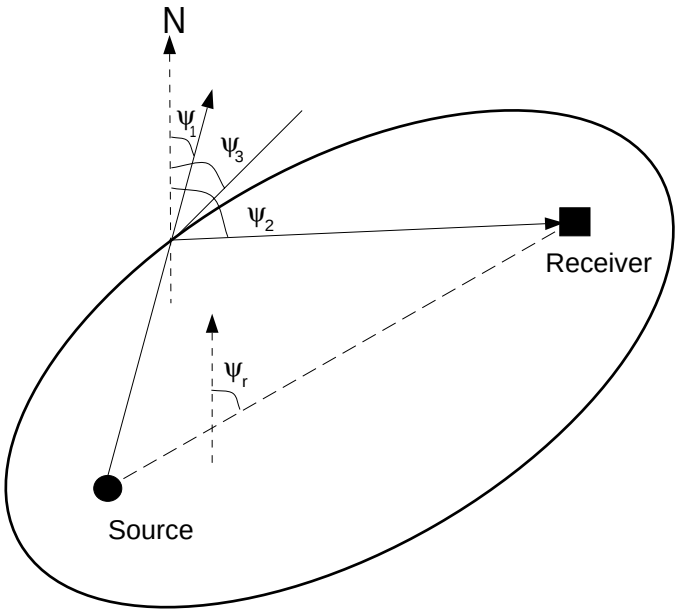

Figure 20. Three definitions of the local azimuth at the scatter: ψ_1 – azimuth between the source and the scatterer, ψ_2 – azimuth between the scatterer and the receiver, and ψ_3 – the average of ψ_2 and ψ_2.

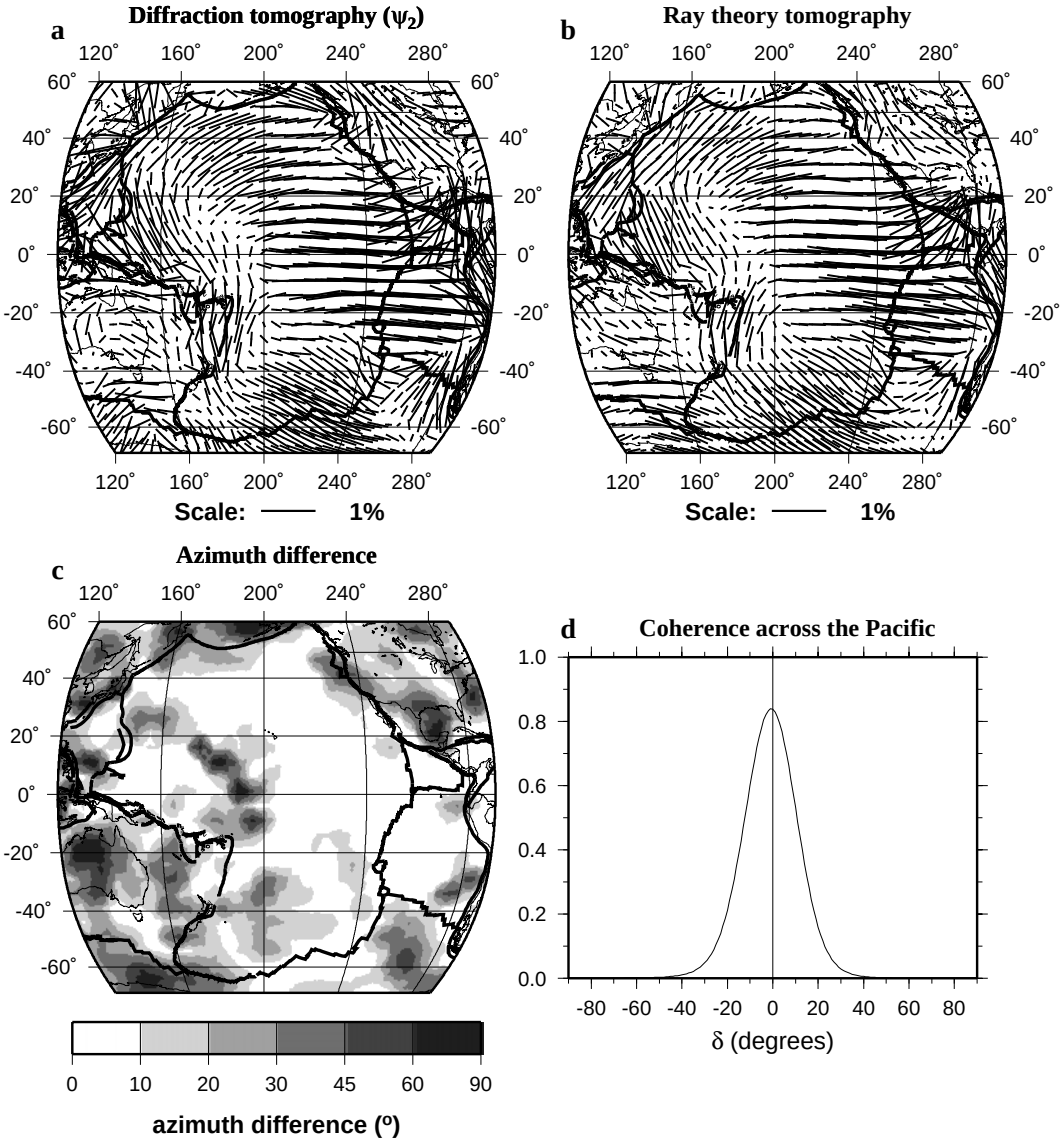

Figure 21. The effect of diffraction through the anisotropic model on estimates of azimuthal anisotropy for the 50 sec Rayleigh wave group speed. (a) Anisotropy results based on diffraction tomography for both the isotropic and anisotropic parts of the model, where the local azimuth at the scatterer is defined as the angle between the scatterer and the receiver (ψ_2 in Fig. 20). (b) Anisotropy results using ray theory for the anisotropic part of the model and diffraction theory for the isotropic aprt. (c) Difference in azimuth between the fast axis directions in (a) and (b). The largest differences occur near plate boundaries, on continents ,and where the amplitude of anisotropy is small (e.g., in parts of the Central Pacific). (d) Coherence between the results in (a) and (b) across the Pacific.